energies

MDPI

Article

Structural Coupling and Layer-Resolved Heat Transfer in a Multilayer Spiral-Wound Heat Exchanger with Molten Salt on the Shell Side

Xing Huang [1], Junjie Chen [1], Taotao Huang [1], Xiaoming Fang [1,2], Ziye Ling [1,2] and Zhengguo Zhang [1,2,*]

[1] Key Laboratory of Heat and Mass Transfer and Low-Carbon Conversion, The Ministry of Education, School of Chemistry and Chemical Engineering, South China University of Technology, Guangzhou 510640, China; 202520123219@mail.scut.edu.cn (X.H.)
[2] Guangdong Engineering Technology Research Center of Efficient Heat Storage and Application, South China University of Technology, Guangzhou 510640, China
* Correspondence: cezhang@scut.edu.cn

Abstract

Geometric modifications in spiral-wound heat exchangers alter flow passages and heat transfer areas, complicating performance interpretation. A three-dimensional numerical study compares 22 circular tube configurations of a three-layer spiral-wound heat exchanger with shell-side molten salt and tube-side water. The shell and core dimensions, tube counts, and inlet conditions are fixed. Actual tube wall areas and layer-resolved heat flux integrals distinguish area and mean heat flux contributions to heat duty changes, alongside the pressure drop and a relative performance evaluation criterion (PEC). Reducing the nominal axial clearance from 2.0 to 1.5 mm changes the heat duty by +2.32%, −3.78%, and +2.89% in three structural configurations. For G01–G21, the area term is +38.31 kW and the mean heat flux term is −60.76 kW, with the net loss concentrated in the outer layer. At a fixed total radial clearance, uniform allocation gives the highest PEC among the cases examined, while an outward-biased allocation can offset inner-layer losses through increased outer-layer heat transfer. Relative to G02, G01 reduces the pressure drop by 54.37% and increases the PEC by 14.20%; G22 gives the highest heat duty, 655.26 kW. These numerical results show that structural selection requires the simultaneous consideration of the actual area, layer-resolved thermal response, and flow resistance within the specified geometric and modeling constraints.

Keywords: molten salt; spiral-wound heat exchanger; structural coupling; layer-resolved heat transfer; thermal hydraulic performance

Academic Editor: Jan Taler

Received: 12 October 2026
Revised: 26 October 2026
Accepted: 4 November 2026
Published: 6 November 2026

Copyright: © 2026 by the authors. Licensee MDPI, Basel, Switzerland. This article is an open access article distributed under the terms and conditions of the Creative Commons Attribution (CC BY) license.

1. Introduction

Molten salt thermal energy storage helps to match an intermittent solar energy supply to the heat demand [1]. Its heat exchangers must deliver the required duty within a limited volume while controlling hydraulic losses and thermal stresses [2,3]. Hood et al. [4] showed that temperature gradients and transient operation also affect the service life of molten salt–steam heat exchangers. Structural design therefore requires a balance between thermal capacity, flow resistance, and temperature distribution.

Molten salt heat transfer enhancement can be pursued through fluid modification or channel design. Huang et al. [5] reviewed both approaches. For internally helically finned

tubes, Huang et al. [6] found that the fin pitch, angle, and height alter heat transfer together with pressure drop. These results establish the importance of hydraulic penalties, but a tube-side enhancement acts within an individual passage. The interconnected shell-side passages of a multilayer bundle additionally permit heat transfer to be redistributed between layers.

Related helical channel studies also show that thermal gains must be assessed alongside hydraulic penalties. Abdelmagied [7] combined a helical coil with an inner twisted tube and developed heat transfer and friction correlations. In a shell and twisted conical coil experiment, Abdelmagied [8] examined the curvature, orientation, and feeding configuration. These studies demonstrate the role of geometry-induced secondary motion, but their correlations concern different passages and reference quantities. The present work instead examines how spacing changes in a smooth multilayer bundle redistribute shell-side heat transfer under fixed inlet conditions.

The shell-side molten salt experiments by Qian et al. [9] and Qiu et al. [10] provide performance data for shell-and-tube and rod baffle configurations. Xie et al. [11] and Khaliquzzama et al. [12] showed that perforated baffles can reduce resistance while sacrificing some heat transfer. Chen et al. [13] combined helical baffles and elliptic tubes to modify the same trade-off for molten salt nanofluids. These studies concern baffle-guided passages or modified tube shapes; smooth circular tube spiral-wound heat exchangers offer a different means of adjusting the available shell-side space through the tube winding and interlayer clearances.

Multilayer spiral-wound heat exchangers (SWHEs) provide a large heat transfer area between the central core and shell through helically wound tube bundles. The tube curvature and arrangement modify the shell-side flow, offering another configuration for compact molten salt heat exchangers. Weikl et al. [14] discussed the applications of this configuration in molten salt systems. Pardillos-Pobo et al. [15] subsequently designed sodium–molten salt and molten salt–supercritical CO_2 SWHEs for chloride-salt thermal storage systems, using a multistream model to describe temperature differences between tube layers. Dong et al. [16] investigated molten salt nanofluids in an SWHE experimentally and numerically, although molten salt flowed on the tube side and thermal oil on the shell side. These studies provide a basis for high-temperature SWHE applications and highlight the need to examine interlayer flow passages and layer-resolved heat transfer when molten salt flows on the shell side.

Shell-side heat transfer and flow resistance in SWHEs have been investigated extensively. Neeraas et al. [17] measured the local heat transfer coefficients and frictional pressure drops for gas flowing on the shell side of an SWHE. Combining experiments and numerical simulations, Lu et al. [18] showed that the choice of tube wall thermal boundary conditions affects shell-side heat transfer predictions. Regarding geometric parameters, Lu et al. [19] examined the tube diameter, layer count, tube spacing, and central core diameter, while Wu et al. [20] investigated the tube diameter, tube spacing, and spacer bar thickness. Mostafazade Abolmaali and Afshin [21] further developed a geometrically consistent parametric model and derived Nusselt number and friction factor correlations accounting for the layer count and dimensionless tube spacing. These studies support performance prediction and indicate that geometric effects should be discussed under clearly defined structural constraints and thermal boundary conditions.

Building on these studies, structural optimization has expanded from single-parameter comparisons to combinations of parameters and local flow control. Wang et al. [22] used response surface methods and a multiobjective genetic algorithm to seek a compromise between the heat transfer coefficient and pressure drop. Their subsequent study of spacer bars showed that staggered arrangements promoted fluid exchange between regions of different velocities and between adjacent tube layers [23]. Duan et al. [24] and Wu

et al. [25] proposed novel spacer bars and helical rods, respectively, to improve the overall performance by reorganizing the shell-side flow. These studies show that flow interaction between tube layers is an important factor affecting performance. For a basic bundle of smooth circular tubes, further clarification is needed on how changes in tube diameter and spacing alone redistribute layer-resolved heat transfer contributions and whether these changes translate into overall performance gains.

Published geometric trends depend on the fluid and design constraints. Gu et al. [26] reported a decrease in the shell-side heat transfer coefficient with increasing tube diameters for a propylene glycol–water mixture. More recently, Wang et al. [27] found an increasing coefficient with the tube diameter and reductions in both the coefficient and pressure drop as the radial or axial spacing increased. Gao et al. [28] connected structural changes to fluid disturbance and boundary layer development. These studies motivate an explicit distinction between a prescribed geometric adjustment and the accompanying changes in actual area and flow passages.

Local analyses help to explain why global performance metrics change. Wang et al. [29] studied the distribution of thermal resistance in a molten salt heat exchanger, and Bi et al. [30] introduced an axial local thermal resistance ratio for SWHE optimization. These approaches locate thermal limitations, while performance evaluation also depends on the constraints used for comparison [31]. A complementary question is how a modification changes the area and mean heat flux of each radial layer and whether a gain in one layer is offset elsewhere.

Under fixed shell and core dimensions, tube diameters and interlayer clearances compete for radial space. An axial spacing adjustment also changes the helical lead, tube length, and actual heat transfer area. Consequently, a larger heat duty cannot automatically be attributed to stronger convection, and an increase in area need not increase the total duty. The unresolved design issue addressed here is how these coupled adjustments redistribute thermal contributions across the layers and alter the heat duty–resistance trade-off.

This study compares 22 smooth circular tube, three-layer SWHE configurations at common molten salt–water inlet conditions. Its contribution is a geometry-constrained, layer-resolved assessment: explicit geometric constraints define the comparisons, actual wall areas and integrated heat fluxes separate the mathematical contributions to duty changes, and the layer totals reveal compensating gains and losses. The decomposition is used as an accounting identity rather than an independent causal model. The numerical procedure is assessed against oil–water experiments, and the present G02 molten salt case is examined for mesh sensitivity. The resulting design candidates are evaluated within this scope, followed by a separate exploratory comparison of inlet flow responses. A local geometric response correlation is additionally examined for the ten configurations with identical 8 mm tube diameters and a fixed 2 mm total radial clearance.

2. Physical Model and Reference Experimental Data

2.1. Heat Exchanger Configuration and Geometric Parameters

The heat exchanger comprises three coaxial layers of helically wound circular tubes (Figure 1). Molten salt flows outside the tubes between the shell and central core, while water flows inside the helical tubes in a counterflow arrangement. The inner, middle, and outer layers contain 4, 6, and 8 tubes, respectively, giving 18 tubes in total. The shell inner diameter is 96 mm, the central core outer diameter is 42 mm, the tube wall thickness is 0.8 mm, and the shell-side axial characteristic length is 0.76 m. The shell and central core boundary dimensions are identical for all configurations. Tube outer diameters of 7, 8, and 9 mm are used, corresponding to inner diameters of 5.4, 6.4, and 7.4 mm, respectively.

Layers are numbered from the inside outward. The symbols d_j, $D_{c,j}$, N_j, and $g_{a,j}$ denote the tube outer diameter, winding center diameter, tube count, and nominal axial clearance, respectively. Radial clearances g_{12} and g_{23} are measured between adjacent tube bundle envelopes. Equation (1) defines the multistart helical lead; the nominal axial clearance is not the minimum distance between curved tube surfaces. Post-processing uses each model's actual outer wall area because structural adjustments change the tube length.

The clearances from the innermost layer to the core and from the outermost layer to the shell are both 0.5 mm. With fixed shell and core dimensions, the sum of the tube diameters and total interlayer clearance obeys Equation (2). This constraint distinguishes diameter arrangement at fixed clearances from coupled changes in diameter and passage space.

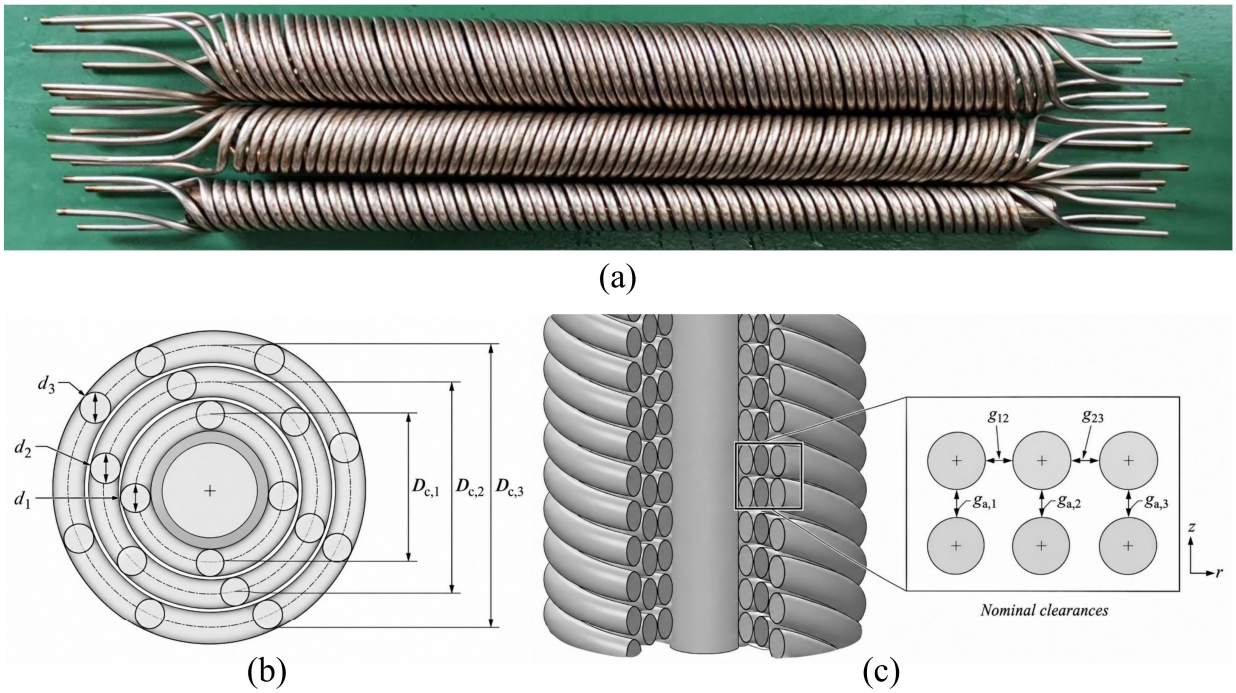


Figure 1. Physical model and geometric parameters of the three-layer spiral-wound heat exchanger. (**a**) Three-layer spiral-wound tube configuration; (**b**) radial cross-section showing d_j and $D_{c,j}$; (**c**) nominal axial clearance within a layer and radial clearances g_{12} and g_{23}.

2.2. Structural Comparison Scheme and Common Operating Conditions

G02 is the reference, with 8/8/8 mm tubes, a uniform 2 mm axial clearance, and 1/1 mm radial clearances (Table 1). G04/G02/G05/G06 compare uniform axial spacing; G07/G02/G08 compare its radial allocation. G09–G12 compare radial clearance allocation at a fixed total, and G13–G16 compare the diameter arrangement at fixed clearances. G01/G19/G20/G02/G03 follow a coupled diameter sum/clearance path. G21 and G22 apply the same axial adjustment to G01 and G14. These sets hold selected inputs constant, but the actual tube length, area, curvature, and passage geometry can still change; the resulting differences are configuration responses.

Table 1. Geometric parameters of the 22 configurations (all dimensions in mm).

Case	Tube Outer Diameter $d_1/d_2/d_3$	Nominal Axial Clearance $g_{a,1}/g_{a,2}/g_{a,3}$	Radial Clearance g_{12}/g_{23}	Winding Center Diameter $D_{c,1}/D_{c,2}/D_{c,3}$
G01	7/7/7	2/2/2	2.5/2.5	50/69/88
G02	8/8/8	2/2/2	1/1	51/69/87
G03	9/8/8	2/2/2	0.5/0.5	52/70/87
G04	8/8/8	1.5/1.5/1.5	1/1	51/69/87
G05	8/8/8	2.5/2.5/2.5	1/1	51/69/87
G06	8/8/8	3/3/3	1/1	51/69/87
G07	8/8/8	1.5/2/2.5	1/1	51/69/87
G08	8/8/8	2.5/2/1.5	1/1	51/69/87
G09	8/8/8	2/2/2	0.5/1.5	51/68/87
G10	8/8/8	2/2/2	0.75/1.25	51/68.5/87
G11	8/8/8	2/2/2	1.25/0.75	51/69.5/87
G12	8/8/8	2/2/2	1.5/0.5	51/70/87
G13	7/8/9	2/2/2	1/1	50/67/86
G14	9/8/7	2/2/2	1/1	52/71/88
G15	7/9/8	2/2/2	1/1	50/68/87
G16	8/7/9	2/2/2	1/1	51/68/86
G17	9/7/9	2/2/2	0.5/0.5	52/69/86
G18	9/8/8	2.5/2/1.5	0.5/0.5	52/70/87
G19	7/7/8	2/2/2	2/2	50/68/87
G20	7/8/8	2/2/2	1.5/1.5	50/68/87
G21	7/7/7	1.5/1.5/1.5	2.5/2.5	50/69/88
G22	9/8/7	1.5/1.5/1.5	1/1	52/71/88

Note: Geometric constraints couple some adjustments to tube length, wall area, and passage dimensions; these comparisons are not all strict single-variable controls.

The 22 configurations in Sections 5.1–5.8 are compared at molten salt and water inlet temperatures of 450 °C and 80 °C and volumetric flow rates of 3 m^3/h and 5 m^3/h, respectively. The volumetric flow rate provides a common description of the operating conditions. When a mass-flow inlet is used, the mass flow rate must be calculated using the corresponding inlet density. Mass flow rates calculated from mean properties during tabular post-processing are quantities used to estimate the heat duty and are treated separately from the solver inlet inputs. This study focuses on structural responses under fixed inlet conditions. The inlet flow rates are varied separately in Section 5.9, where the corresponding ranges are specified.

2.3. Previously Obtained Oil–Water Data

No new molten salt–water experiments were performed in this study. The numerical procedure was assessed using previously obtained oil–water measurements from a multilayer spiral-wound prototype. These measurements were acquired on the circulation and measurement platform described by Chen et al. [32], comprising thermal oil and cooling water loops and a data acquisition system for the temperatures, flow rates, and pressure drop. The tested prototype shares the multilayer spiral-wound arrangement of the present model, but its dimensions differ from those of G02, as summarized in Section 4.4.

Water is used as the cold-side heat-absorbing fluid, with Kunlun L-QC310 organic thermal oil as the hot-side heat transfer fluid. During the experiments, the tube-side cooling water inlet temperature ranges from 35 °C to 60 °C, with a volumetric flow rate of 2.9 m^3/h to 5.0 m^3/h. The shell-side thermal oil inlet temperature ranges from 55 °C to 80 °C, with a volumetric flow rate of 3.0 m^3/h to 6.5 m^3/h. Over the experimental temperature

range of 55 °C to 80 °C, the thermal oil remains a stable liquid, with smoothly varying thermophysical properties and flow characteristics. The property ranges are listed in Table 2.

Table 2. Thermophysical properties of the thermal oil over 55–80 °C.

Thermophysical Property	Unit	Value
Density	kg/m³	959~997
Specific heat capacity	kJ/(kg·K)	1.88~2.05
Thermal conductivity	W/(m·K)	0.1021~0.1041
Kinematic viscosity	mm²/s	2.567~9.111

3. Data Processing and Performance Evaluation Methods

The outer tube wall heat duty is the primary thermal quantity. Actual areas, model-specific velocities, and mean properties are used to calculate the overall and equivalent shell-side heat transfer coefficients and performance metrics. Matched configurations are then compared through layer-resolved heat duty decomposition. Unless mm is explicitly indicated in Table 1 or Equation (2), geometric dimensions are substituted in m, heat duty in W, and pressure drop in Pa.

3.1. Geometric Constraints and Thermophysical Property Treatment

Equation (1) gives the helical lead of each layer. The 26 mm in Equation (2) is the radial shell-to-core space of 27 mm minus two boundary clearances of 0.5 mm. This is a geometric constraint, not an empirical correlation between independent variables.

$$P_j = N_j(d_j + g_{a,j}) \tag{1}$$

$$d_1 + d_2 + d_3 + g_{12} + g_{23} = 26\ \text{mm} \tag{2}$$

The reference temperature for fluid properties is the arithmetic mean of the inlet and outlet temperatures:

$$T_{m,k} = \frac{T_{\text{k,in}} + T_{\text{k,out}}}{2} \tag{3}$$

Here, k denotes molten salt (s) or water (w). Table 3 records the molten salt values used in spreadsheet post-processing, with linear interpolation according to Equation (4). For the 22 structural cases, the mean reference temperature is 296.44–315.01 °C, so this particular two-point table is extrapolated by at most 3.6 °C below 300 °C. Its constant density of 1802.9 kg/m³ is a reference value adopted for processing the flow rate. This two-point approximation is separate from the complete material model used in Fluent and does not establish its temperature range of validity.

$$\varphi(T_m) = \varphi(T_a) + \frac{\varphi(T_b) - \varphi(T_a)}{T_b - T_a}(T_m - T_a) \tag{4}$$

The shell-side fluid is the base quaternary nitrate salt containing $Ca(NO_3)_2{\cdot}4H_2O$, KNO_3, $NaNO_3$, and $NaNO_2$, without added nanoparticles. Its property data are discussed by Huang et al. [6] and traced to the base salt measurements in Zhang et al. [33]; the nanofluid mixtures in this source are not used here. The source curves cover 200–500 °C for specific heat and thermal conductivity and approximately 250–450 °C for viscosity. Temperature-dependent values were extended by linear extrapolation before being entered into Fluent. The G02 salt outlet temperature of 151.05 °C falls below the source ranges, so the extrapolated values extend the computational model rather than the exper-

imental validity of the measurements. Their influence has not been independently quantified. The local material model is distinct from the mean property post-processing approximation in Table 3.

Water is modeled in Fluent using the database liquid-water material with constant properties. The separate equivalent water properties used in spreadsheet post-processing are 958.37 kg/m^3, 2.8166 × 10^{-4} Pa·s, 4210 J/(kg·K), and 0.67720 W/(m·K) for the density, dynamic viscosity, specific heat, and thermal conductivity, respectively. They are reference values for heat duty estimates and equivalent thermal resistance separation, not the temperature-dependent inputs of the CFD solver. This distinction also limits the interpretation of fluid-side energy estimates as a solver energy balance check.

Table 3. Reference data for calculating mean molten salt properties.

Property Used in Post-Processing	300 °C	350 °C	Unit
Molten salt density	1802.9	1802.9	kg/m^3
Molten salt specific heat capacity	1350	1380	J/(kg·K)
Molten salt thermal conductivity	0.33	0.38	W/(m·K)
Molten salt dynamic viscosity	0.00405	0.00300	Pa·s

3.2. Heat Duty and Overall Heat Transfer Coefficient

Fluid-side heat duties estimated with mean properties provide an auxiliary check using Equation (5). Volumetric flow rates are substituted in m^3/s, requiring division by 3600 for values in m^3/h. For the temperature-dependent specific heat, an enthalpy flow difference is required for a rigorous energy balance; a discrepancy in the mean property estimate does not directly indicate solver energy imbalance.

$$\begin{aligned} \dot{m}_k &= \rho_k V_k \\ Q_{s,est} &= \dot{m}_s c_{p,s}(T_{\mathrm{s,in}} - T_{\mathrm{s,out}}) \\ Q_{w,est} &= \dot{m}_w c_{p,w}(T_{\mathrm{w,out}} - T_{\mathrm{w,in}}) \end{aligned} \quad (5)$$

The average of the estimated fluid-side heat duties is not used as the primary heat duty. The layer heat duty is obtained by integrating the total heat flux over the selected outer tube walls, equivalently multiplying the area-weighted mean heat flux by the actual area:

$$Q_j = \int q''_j dA = \bar{q}''_j A_j \; ; \; Q = Q_1 + Q_2 + Q_3 \quad (6)$$

In Equation (6), heat transfer from salt to water is positive. A_j contains exactly the surfaces used for layer-j heat flux integration. Equation (7) gives the total outer and inner areas used in thermal resistance separation, where $d_{i,j}$ denotes the tube inner diameter.

$$A_o = \sum A_j \; ; \; A_i = \sum A_j \frac{d_{i,j}}{d_j} \quad (7)$$

The counterflow logarithmic mean temperature difference uses positive terminal differences; their common value applies when they are equal. The overall heat transfer coefficient is based on the actual outer wall area:

$$\Delta T_{lm} = \frac{\Delta T_1 - \Delta T_2}{ln(\Delta T_1/\Delta T_2)} \; ; \; \Delta T_1 = T_{\mathrm{s,in}} - T_{\mathrm{w,out}} \quad (8)$$

In Equation (8), the temperature difference at the other end, ΔT_2, is the molten salt outlet temperature minus the water inlet temperature. All outlet temperatures are evaluated using the same post-processing procedure.

$$U_o = \frac{Q}{A_o \Delta T_{lm}} \tag{9}$$

3.3. Equivalent Tube-Side Heat Transfer Coefficient and Shell-Side Thermal Resistance Separation

A single Reynolds number based on the total tube-side flow area and tube count-weighted mean inner diameter gives a base Nusselt number, followed by a curvature correction for each layer. This equivalent treatment supports thermal resistance separation. Equal mass flow is prescribed at the individual tube inlets (Section 4.2), but the equivalent coefficient does not resolve differences in local tube-side heat transfer among mixed-diameter branches.

$$A_{f,w} = \sum \frac{N_j \pi {d_{i,j}}^2}{4} \; ; \; \bar{d}_i = \frac{\sum N_j d_{i,j}}{18} \; ; \; u_w = \frac{V_w}{A_{f,w}} \tag{10}$$

$$Re_w = \frac{\rho_w u_w \bar{d}_i}{\mu_w} \; ; \; Pr_w = \frac{\mu_w c_{p,w}}{\lambda_w} \tag{11}$$

$$f_i = (1.82\, log_{10} Re_w - 1.64)^{-2} \tag{12}$$

Equation (13) uses the Gnielinski form [34] without a finite length correction, consistently with the adopted post-processing. The internal heat transfer coefficient is averaged by the tube count in Equation (15).

$$Nu_b = \frac{(f_i/8)(Re_w - 1000)Pr_w}{1 + 12.7(f_i/8)^{1/2}({Pr_w}^{2/3} - 1)} \tag{13}$$

Equation (14) applies the layer-specific curvature correction, with $R_{c,j}$ equal to half the winding center diameter in Table 1. It is part of the equivalent model, not a correlation calibrated for flow splitting among these branches.

$$C_{r,j} = 1 + 10.3\left(\frac{d_{i,j}}{R_{c,j}}\right)^3 \; ; \; h_{i,j} = \frac{Nu_b C_{r,j} \lambda_w}{d_{i,j}} \tag{14}$$

$$h_i = \frac{\sum N_j h_{i,j}}{18} = \frac{4h_{i,1} + 6h_{i,2} + 8h_{i,3}}{18} \tag{15}$$

The wall conductivity is 15 W/(m·K). Equation (16) uses the tube count-weighted mean outer and inner diameters to estimate an equivalent wall resistance based on the outer area, rather than solving the parallel resistances of individual layers.

$$\bar{d}_o = \frac{\sum N_j d_j}{18} \; ; \; R''_{wall,o} = \frac{\bar{d}_o}{2\lambda_{wall}} ln\left(\frac{\bar{d}_o}{\bar{d}_i}\right) \tag{16}$$

$$\frac{1}{h_o} = \frac{1}{U_o} - \frac{A_o}{A_i h_i} - R''_{wall,o} \tag{17}$$

Equation (17) yields the equivalent shell-side heat transfer coefficient. The directly integrated heat duty, actual area, and pressure drop are retained in the comparisons to avoid interpreting small differences in the equivalent water-side estimate as established local heat transfer effects.

At the G02 values, differentiating Equation (17) at a fixed geometry gives relative sensitivities of h_o of approximately +1.620 to U_o, −0.315 to h_i, and +0.306 to $R''_{wall,o}$. For example, a 1% perturbation in one input, with the others fixed, changes h_o by approximately +1.62%, −0.315%, or +0.306%, respectively. These local post-processing sensitivities identify possible amplification in the inferred coefficient; they are neither measured errors nor the response to changing a CFD material input.

3.4. Shell-Side Performance Metrics and Layer-Resolved Evaluation

The shell-side equivalent diameter uses the fluid-domain volume V_s and total outer tube wall area A_o. Both are extracted over consistently defined model extents. The resulting volume-to-heat-transfer-area length is

$$D_e = \frac{4V_s}{A_o} \tag{18}$$

Equation (18) excludes the shell and core from its area denominator, unlike a conventional hydraulic diameter based on all wetted surfaces. Equation (19) uses the maximum velocity u_{max} in the entire shell-side domain and the axial characteristic length L_s = 0.76 m:

$$f_o = \frac{2\Delta p D_e}{\rho_s {u_{max}}^2 L_s} \tag{19}$$

Here, Δp is the inlet-to-outlet static-pressure difference in Pa, including losses associated with the bundle, turning, and collection regions within the specified domain. The reference velocity is a domain maximum rather than a bulk channel velocity. Therefore, f_o is an apparatus-level resistance index, not a fully developed pipe friction coefficient. Comparison with conventional correlations requires consistent definitions of the velocity, diameter, pressure loss extent, and Darcy or Fanning normalization. A localized maximum is also more sensitive to the mesh resolution than an integral flow quantity.

$$Nu_o = \frac{h_o D_e}{\lambda_s} \tag{20}$$

$$J = \frac{Nu_o}{{f_o}^{1/3}} \; ; \; PEC = \frac{J}{J_0} = \frac{Nu_o/Nu_{o,0}}{(f_o/f_{o,0})^{1/3}} \tag{21}$$

The subscript 0 denotes G02. The one-third exponent is retained as a conventional thermal–hydraulic screening form [31], but its equal-pumping-power interpretation requires a compatible geometry and flow normalization. Since D_e and u_{max} vary here, the PEC is a dataset-specific ranking index, not an equal-power enhancement factor or an energy saving percentage. It is therefore interpreted together with Q, Δp, and the actual area. At a specified volumetric flow rate, the nominal shell-side hydraulic power is calculated as the flow rate multiplied by the pressure drop. The pump shaft power additionally requires the pump efficiency; the total circulation power also requires the water-side and external-loop losses.

The supplementary indices in Section 5.9 retain this dataset's own normalization and are used to examine flow-rate responses separately from the structural PEC defined here.

$$\eta_{Q,j} = \frac{Q_j}{Q} \; ; \; \eta_{A,j} = \frac{A_j}{A_o} \tag{22}$$

$$R_j = \frac{\eta_{Q,j}}{\eta_{A,j}} = \frac{\bar{q}''_j}{Q/A_o} \tag{23}$$

The fractions $\eta_{Q,j}$ and $\eta_{A,j}$ describe the layer heat duty and area. An R_j above unity means that the layer's mean wall heat flux exceeds the overall mean. It reflects both local temperature differences and convective transport, not a separate layer heat transfer coefficient. The outer clearance fraction at a fixed total radial clearance is

$$\chi = \frac{g_{23}}{g_{12} + g_{23}} \tag{24}$$

3.5. Decomposition of Contributions to Heat Duty Changes

For matched configurations, a and b denote the states before and after an adjustment, distinct from reference case 0 (G02). Equation (6) gives the following symmetric decomposition of the layer heat duty difference:

$$\Delta Q_j = Q_{j,b} - Q_{j,a} = C_{A,j} + C_{q,j} \tag{25}$$

$$C_{A,j} = \frac{\bar{q}''_{j,b} + \bar{q}''_{j,a}}{2}(A_{j,b} - A_{j,a}) \tag{26}$$

$$C_{q,j} = \frac{A_{j,b} + A_{j,a}}{2}(\bar{q}''_{j,b} - \bar{q}''_{j,a}) \tag{27}$$

$$\Delta Q = \sum \Delta Q_j = \sum C_{A,j} + \sum C_{q,j} \tag{28}$$

$C_{A,j}$ and $C_{q,j}$ are the area change and mean heat flux change terms, in W. The arithmetic mean of each quantity across the two configurations allocates their product change symmetrically, so the terms sum exactly to ΔQ_j. They do not represent separate experiments in which the area or convection alone changes. In particular, the heat flux term includes the local fluid and wall temperatures, boundary-layer transport, and the influence of tube-side heat removal. It cannot identify a unique flow mechanism without additional local evidence.

Taking the ratio of Equation (9) between two states with positive heat duties and then the natural logarithm gives

$$ln\frac{Q_b}{Q_a} = ln\frac{U_{o,b}}{U_{o,a}} + ln\frac{A_{o,b}}{A_{o,a}} + ln\frac{\Delta T_{lm,b}}{\Delta T_{lm,a}} \tag{29}$$

Equation (29) is additive in logarithms, not in ordinary percentage changes. Since U_o is derived from the same heat duty, area, and temperature difference, this relation is a consistency check rather than independent thermal validation.

3.6. Local Geometric Response Correlations

The correlation subset comprises G02 and G04–G12. All ten cases have 8/8/8 mm tubes; the same shell, core, layer tube counts, and inlet conditions; and a total radial clearance of 2 mm. G02 and G04–G08 also share winding center diameters of 51/69/87 mm. In G09–G12, the middle-layer winding diameter changes with radial clearance allocation and is not an additional independent input. Three dimensionless descriptors distinguish the mean axial clearance, its outward allocation, and radial clearance allocation:

$$\overline{g_a} = \frac{g_{a,1} + g_{a,2} + g_{a,3}}{3}; \quad \xi = \frac{\overline{g_a} - g_{a,0}}{g_{a,0}}$$
$$\zeta = \frac{g_{a,3} - g_{a,1}}{g_{a,0}}; \quad \psi = \frac{g_{23} - g_{12}}{g_{23} + g_{12}} \tag{30}$$

Here, $g_{a,0}$ = 2 mm is the nominal axial clearance of G02. A positive ζ denotes increasing axial clearance toward the outer layer; a positive ψ denotes a larger outer radial gap, and $\psi = 2\chi - 1$. The response y denotes either Nu_o or f_o, with y_0 its G02 value. The following low-order form retains directional terms and allows a nonmonotonic radial allocation response:

$$\frac{y}{y_0} = c_0 + c_1\xi + c_2\zeta + c_3\psi + c_4\psi^2 \tag{31}$$

The five coefficients are estimated by ordinary least squares on the ten CFD-derived responses. The intercept is fitted freely, so normalization does not force the fitted curve

through G02. A quadratic radial term represents the observed departure from uniform allocation; no interaction terms are fitted because simultaneous changes along the different paths were not sampled. Leave-one-out cross-validation refits the same expression to nine cases and predicts the omitted case, repeating this for all ten cases. The reported errors are absolute relative deviations from the CFD-derived values. This internal prediction check is separate from experimental validation and from numerical uncertainty. No machine learning training or independent testing dataset is used.

Applicability is restricted to the three sampled paths: uniform axial clearance of 1.5–3.0 mm with both radial gaps at 1 mm; the linear axial clearance distributions represented by G07/G02/G08; and radial allocation with each axial clearance at 2 mm and the total radial clearance at 2 mm. The tube length, actual area, and passage changes remain included in these configuration responses. The expression is not validated for combined adjustments, mixed tube diameters, or different inlet conditions, and it does not identify independent Reynolds or Prandtl number exponents.

4. Numerical Simulation Methods

4.1. Solution Model and Basic Assumptions

ANSYS Fluent 2022 R1 solves the three-dimensional steady Reynolds-averaged flow and heat transfer with a pressure-based solver, the realizable k–ε turbulence model, and enhanced wall treatment. The molten salt material uses temperature-dependent properties, while water uses constant database properties. Steady RANS is adopted to compare nominal mean operating states at fixed inlet conditions; all time derivatives in the general equations below are set to zero. The convergence of these calculations does not establish the absence of physical fluctuations or describe start-up behavior. Both fluids are treated as single-phase liquids.

Continuity equation:

$$\frac{\partial \rho}{\partial t} + \frac{\partial (\rho u_i)}{\partial x_i} = 0 \tag{32}$$

Momentum equation:

$$\frac{\partial (\rho u_i)}{\partial t} + \frac{\partial \left(\rho u_i u_j\right)}{\partial x_j} = -\frac{\partial p}{\partial x_i} + \frac{\partial \tau_{ij}}{\partial x_j} + \rho g_i + F_i \tag{33}$$

Energy equation:

$$\frac{\partial (\rho h)}{\partial t} + \frac{\partial \left(\rho u_j h\right)}{\partial x_j} = \frac{\partial}{\partial x_j}\left(\lambda_{eff} \frac{\partial T}{\partial x_j}\right) + S_h \tag{34}$$

Turbulent kinetic energy equation:

$$\frac{\partial (\rho k)}{\partial t} + \frac{\partial \left(\rho k u_j\right)}{\partial x_j} = \frac{\partial}{\partial x_j}\left(\left(\mu + \frac{\mu_t}{\sigma_k}\right)\frac{\partial k}{\partial x_j}\right) + G_k + G_b - \rho\varepsilon - Y_M \tag{35}$$

Turbulent kinetic energy dissipation rate equation:

$$\begin{aligned} \frac{\partial (\rho \varepsilon)}{\partial t} + \frac{\partial (\rho \varepsilon u_j)}{\partial x_j} &= \frac{\partial}{\partial x_j}\left(\left(\mu + \frac{\mu_t}{\sigma_\varepsilon}\right)\frac{\partial \varepsilon}{\partial x_j}\right) \\ &+ \rho C_1 S\varepsilon - \rho C_2 \frac{\varepsilon^2}{k + \sqrt{\nu\varepsilon}} + C_{1\varepsilon}\frac{\varepsilon}{k} C_{3\varepsilon} G_b \end{aligned} \tag{36}$$

The 0.8 mm tube wall is represented by thermal resistance with conductivity 15 W/(m·K), retaining conduction normal to the wall. The shell is adiabatic, and fluid–wall interfaces are no-slip. This treatment reduces the mesh required for the solid wall but

omits axial and circumferential heat spreading. A full-length axial conduction scale, using 18 tubes at the largest diameter of 9 mm, a metal path length of 0.76 m, and the full inlet temperature difference of 370 K, is approximately 2.7 W. This scale is small compared with the approximately 600 kW duty and supports neglecting end-to-end wall heat leakage; it does not bound local circumferential or short-length spreading effects.

Buoyancy is omitted in the baseline forced convection model. Imposed circulation motivates this approximation, but a high domain-maximum velocity does not establish negligible buoyancy in slow passages. No quantitative bound on its effect is assigned. The realizable k–ε closure and thin-wall treatment likewise define the present model scope; temperature-dependent transport and circumferential wall gradients may affect its local predictions.

4.2. Boundary Conditions and Discretization

Table 4 summarizes the common boundary conditions for the 22 structural configurations. Outlet extensions reduce boundary effects on bundle flow. The inlet and outlet sections are defined consistently for evaluating the pressure drop, fluid volume, and wall heat duty.

For the 22 structural cases, the total water mass flow rate is divided equally among the 18 individual tube inlets, so each tube receives one eighteenth of the total. The inner, middle, and outer layers consequently receive 4/18, 6/18, and 8/18 of the total flow, respectively. This is a prescribed inlet distribution, not a flow split calculated from a common pressure boundary. Different tube diameters can still produce different inlet velocities. All structural comparisons use this distribution; pressure-driven branch maldistribution is outside the present model.

The Coupled algorithm, PRESTO! pressure interpolation, and second-order upwind momentum and energy discretization are used. Convergence requires flow residuals below 10^{-6} and an energy residual below 10^{-8}, together with a stable total wall heat duty, shell-side pressure drop, and outlet temperatures.

Table 4. Boundary conditions and common model settings for the structural comparison.

Item	Shell Side	Tube Side
Fluid	Base quaternary nitrate salt	Liquid water
Inlet temperature	450 °C	80 °C
Nominal total volume flow	3 m^3/h	5 m^3/h
Inlet flow prescription	Specified total inlet flow	Equal mass flow at all 18 tube inlets
Layer flow allocation	Resolved within the connected shell domain	4/18, 6/18, and 8/18 of total mass flow
Outlet boundary	Pressure outlet	Pressure outlet
Flow arrangement	Counterflow relative to tube-side water	Counterflow relative to shell-side salt
Tube wall interface	No slip; 0.8 mm thermal resistance wall	No slip; conductivity 15 W/(m·K)
External heat loss	Adiabatic shell	No imposed external heat loss
Material treatment	Temperature-dependent; linear extrapolation outside source data	Constant Fluent database properties

Note: Nominal volume flows describe the imposed operating conditions. Conversion to solver mass-flow inputs uses the relevant inlet density; the mean property mass flows used in post-processing are not substituted for these inlet inputs.

4.3. Mesh Selection and Sources of Uncertainty

The unstructured mesh is refined near walls and narrow passages. Five meshes are compared for the present G02 molten salt–water configuration under the inlet conditions in Section 2.2 (Figure 2 and Table 5). Refinement from 11,736,100 to 13,684,500 cells

changes the molten salt outlet temperature by 0.29 K, while the shell-side pressure drop is unchanged at the reported precision. The mesh with 11,736,100 cells is selected to balance the computational cost and the stability of these monitored quantities.

The uncertainty assessment separates numerical discretization, experimental measurement uncertainty, material and boundary inputs, and model-form assumptions. The final mesh increment measures the sensitivity of the monitored G02 quantities to further refinement; it is not a bound on the total uncertainty. Common numerical settings and post-processing definitions provide a consistent basis for comparing configurations but do not establish the cancellation of their errors. The thermal resistance sensitivities in Section 3.3 quantify the local response of the inferred coefficient to its inputs; without input uncertainty estimates, they do not define confidence intervals.

Property and boundary input errors can affect thermal capacity rates, viscosity, and local heat transfer; no perturbed-input CFD ensemble is available to quantify these effects. Turbulence closure adds a separate model-form uncertainty. Li et al. [35] demonstrated the importance of closure calibration in a buoyant low-Prandtl-number liquid-metal flow; this different fluid regime provides a methodological caution, not an error estimate for nitrate salt. Consequently, small differences between the present configurations are reported without statistical significance or a universal error threshold.

Experimental measurement uncertainty applies to the previously obtained oil–water benchmark data. No molten salt experimental uncertainty is assigned because no molten salt measurements were collected. A complete uncertainty budget for the oil–water data would require instrument calibration and repeatability information, together with propagation through the calculated quantities; the available comparison records do not establish this budget. Accordingly, the experiment–simulation deviations in Section 4.4 are reported as benchmark discrepancies, which include both measurement and model effects, rather than as instrument uncertainties or uncertainty bounds for the molten salt predictions.

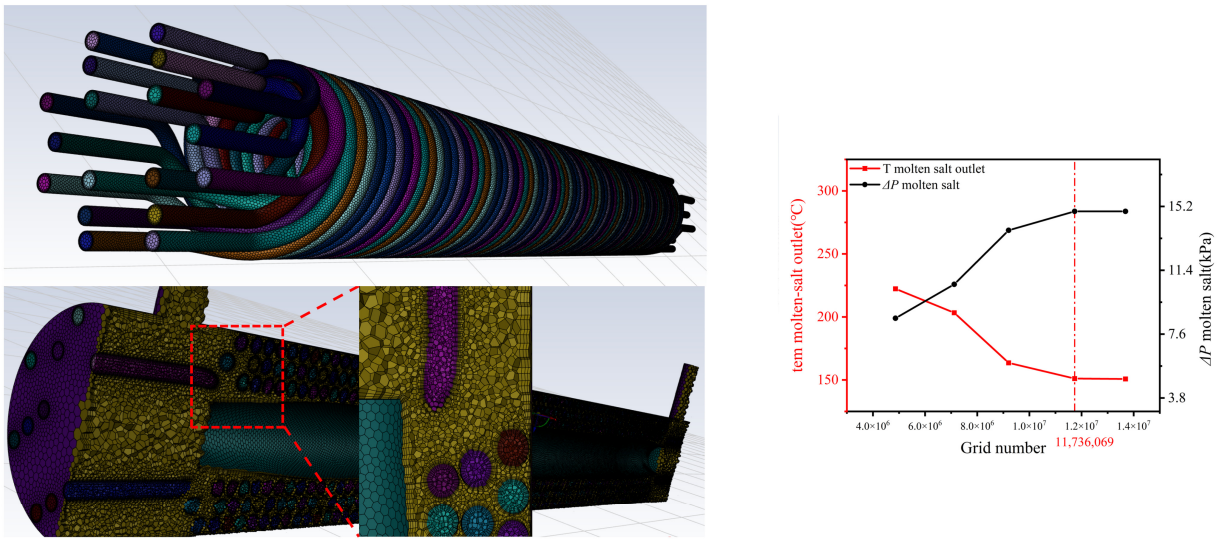


Figure 2. Computational mesh and mesh sensitivity assessment for G02 under the present molten salt–water conditions. (**a**) Overall and near-wall meshes; (**b**) molten salt outlet temperature and shell-side pressure drop versus cell count. In (**a**), the dashed outline and connecting lines identify the enlarged mesh region. In (**b**), the vertical dashed line marks the selected mesh of 11,736,100 cells.

Table 5. Mesh sensitivity of G02 under the present molten salt–water conditions.

Number of Cells	Salt Outlet Temperature (°C)	Shell-Side Pressure Drop (kPa)	Estimated Salt-Side Heat Duty (kW)
4,864,756	222.34	8.545	469.18
7,118,755	203.33	10.564	506.24
9,204,963	163.56	13.78	582.73
11,736,100	151.05	14.91	606.49
13,684,500	150.76	14.91	607.04

4.4. Oil–Water Benchmark Comparison and Application to Molten Salt

The oil–water experimental prototype and G02 share the same three-layer spiral-wound arrangement, with four, six, and eight circular tubes of an 8 mm outer diameter around a 42 mm core. This shared configuration provides a relevant test of coupled flow and heat transfer in a wound-tube bundle. However, the winding center diameters, helical pitches, and radial clearances differ (Table 6). The experimental comparison therefore assesses the numerical procedure for the tested prototype rather than directly validating G02.

Table 6. Main geometric parameters of the previous experimental prototype and G02.

Parameter (mm)	Previous Experimental Prototype	G02 in This Study
Tube inner diameter	6.6/6.4/6.4	6.4/6.4/6.4
Winding center diameter	51/67.2/83.3	51/69/87
Shell inner diameter	95	96
Pitch of an individual helical tube	42/59/73	40/60/80
Two radial clearances	0.10/0.05	1.00/1.00

Note: Layer-specific parameters are listed in the order of the inner, middle, and outer layers. The helical pitch of G02 is calculated from the tube count and nominal axial clearance in each layer; radial clearances are calculated between the envelope surfaces of adjacent tube layers.

The 28 previously obtained comparison records for the SWHE prototype in Table 6 cover the oil and water inlet temperatures and flow rates specified in Section 2.3. Figure 3 compares the measured outlet temperatures and shell-side pressure drops with the corresponding simulations of this prototype; dashed lines indicate exact agreement.

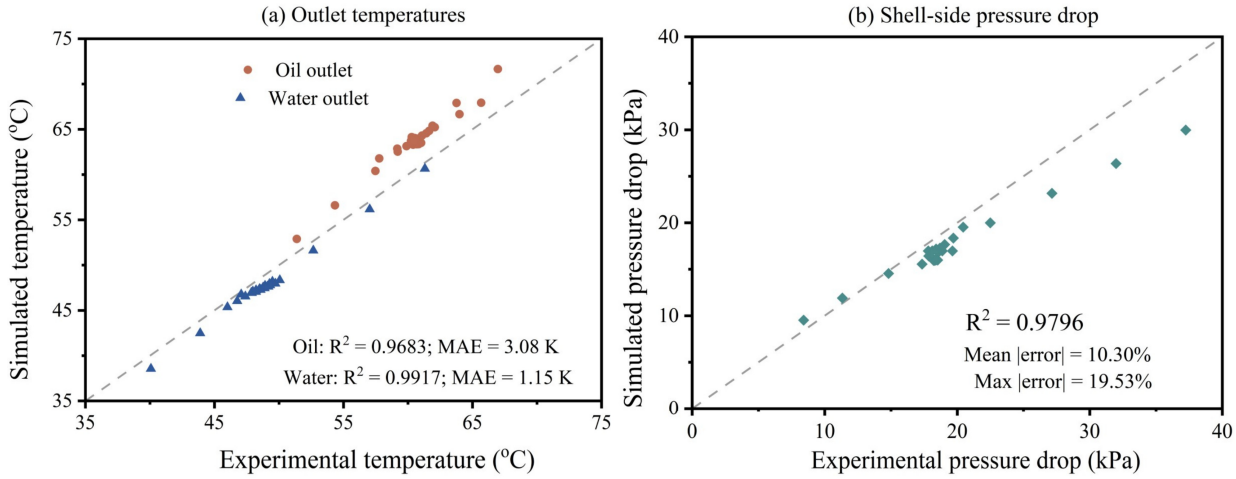


Figure 3. Previous oil–water experiments and corresponding simulations: (**a**) outlet temperatures; (**b**) shell-side pressure drop. R^2 comes from linear regression with an intercept. The tested prototype

differs geometrically from G02 and does not use molten salt. Dashed diagonals indicate exact agreement.

The mean absolute outlet temperature deviations are 3.08 K for oil and 1.15 K for water, with maxima of 4.68 and 1.75 K. The mean and maximum relative pressure drop deviations are 10.30% and 19.53%. The oil outlet temperatures are generally overpredicted, the water temperatures are underpredicted, and the pressure drop underprediction grows at higher oil flow rates. The comparison provides experimental evidence for the numerical procedure within the tested oil–water conditions, while also identifying systematic deviations that should be considered when interpreting its predictions.

For the molten salt study, the governing equation framework and numerical strategy are retained, while the geometry, boundary conditions, and hot-side material inputs are specified for the present cases; water uses constant database properties. The molten salt results are calculated from this model and are not extrapolated experimental measurements. The oil–water comparison provides supporting evidence for the numerical procedure within the tested conditions, while the G02 mesh study separately assesses the spatial resolution under molten salt conditions. These complementary checks support a comparative numerical investigation, but differences in fluid properties, temperature range, and geometry prevent the transfer of the oil–water error bounds to molten salt. The design trends are interpreted within the stated model assumptions; their absolute accuracy remains to be established by direct molten salt experiments.

5. Effects of Structural Parameters on Heat Transfer and Flow Performance

The overall metrics quantify the heat duty and resistance, while layer-resolved results locate gains and losses. The following comparisons account for the actual area and distinguish the tube diameter arrangement from coupled changes in diameter and radial passage space. Nu_o, Q, and U_o describe different aspects of the response because the area, equivalent diameter, and mean properties also vary.

5.1. Typical Flow Characteristics of the Heat Exchanger

Figure 4 illustrates the inlet distribution, bundle flow, and outlet collection for G01, which has tube diameters of 7/7/7 mm, radial clearances of 2.5/2.5 mm, and nominal axial clearances of 2/2/2 mm. G01 represents a low-pressure-drop configuration, while G02 remains the quantitative reference.

The flow changes direction after entering the end chamber and converges toward the outlet nozzle. The local passage geometry produces a nonuniform velocity field, with apparent recirculation near some tube segments. Low-velocity regions coexist with faster passages, so the maximum velocity alone cannot characterize shell-side transport.

The sections contain both fluids: the velocities inside circular tube sections belong to water and do not indicate shell-side disturbance. Shell-side interpretation is restricted to the spaces outside the tubes. This flow overview supports subsequent analysis but does not by itself establish a performance advantage for G01.

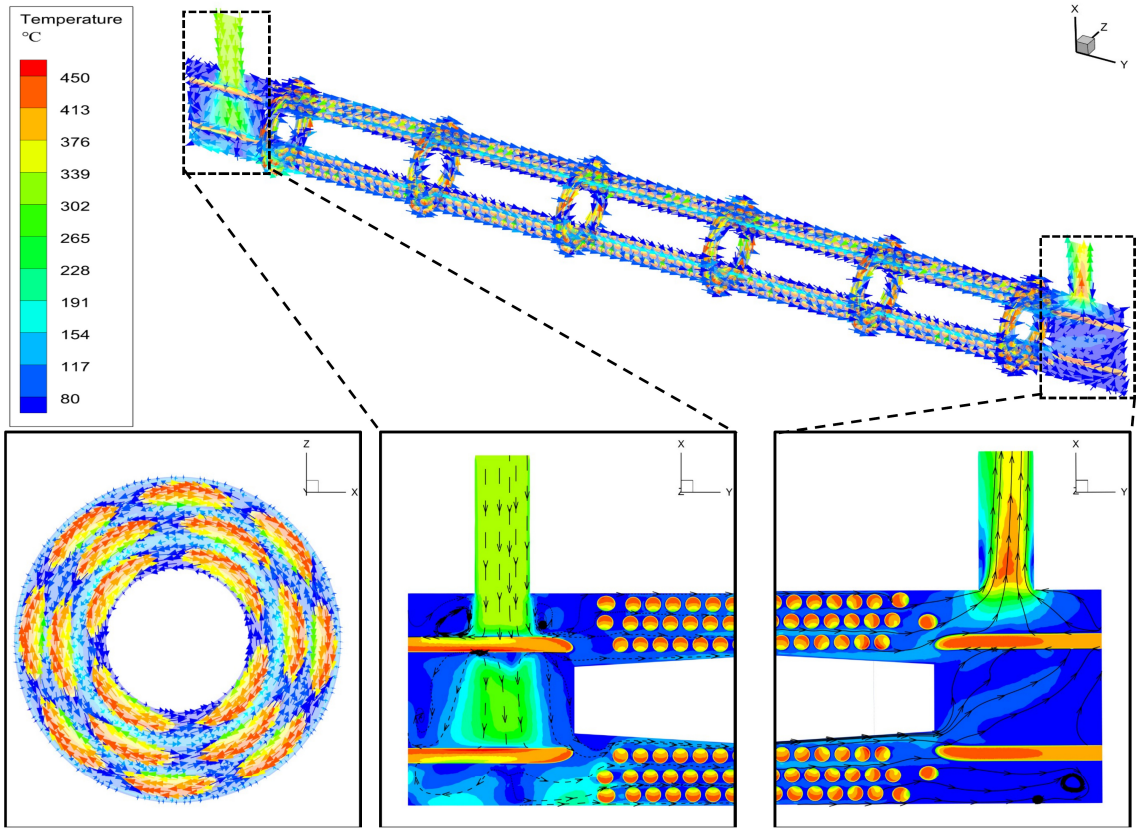


Figure 4. Overall and local flow distributions in G01. Arrow direction indicates flow direction and color indicates temperature. Below, from left to right, are a radial section and enlarged inlet and outlet views (dashed callouts). The sections include both water inside the tubes and molten salt outside them; the interpretation of shell-side flow is restricted to the region outside the tubes.

5.2. Effect of Uniform Axial Tube Spacing

G04, G02, G05, and G06 have uniform nominal axial clearances of 1.5, 2, 2.5, and 3 mm, respectively, with tube diameters of 8/8/8 mm and radial clearances of 1/1 mm (Figure 5). Reducing the clearance from 3 to 1.5 mm raises the heat duty from 566.81 to 645.34 kW, the pressure drop from 11.041 to 17.576 kPa, and the actual outer wall area from 1.263160 to 1.437194 m². The 13.85% heat duty gain accompanies a 13.78% area increase and a 59.19% pressure drop increase.

Relative to G02, G04 has a 4.74% larger area and 2.32% greater heat duty but 2.31% lower mean heat flux; U_o rises by only 1.08%. Thus, the heat duty gain is not wholly an improvement per unit area. Tighter axial packing changes the helical tube length and passage geometry, potentially increasing obstruction and flow losses. Such changes can affect near-wall renewal [28], but their thermal effect must be assessed using the actual layer responses.

G04 increases the pressure drop by 17.88% relative to G02 and has a PEC = 0.9119. G06 reduces the heat duty by 10.13% and pressure drop by 25.95%, with a PEC = 0.9679; G05 has a PEC = 0.9586. G02 gives the highest computed PEC in this set, whereas larger clearances offer lower-pressure-drop alternatives. These rankings refer to the tested spacing range and the normalization in Section 3.4.

Nu_o decreases from 141.21 in G02 to 133.87 in G04, although the inferred h_o rises from 5134.99 to 5225.16 W/(m²·K). Changes in the equivalent diameter and properties explain why Nu_o need not follow h_o or the heat duty. Section 5.7 quantifies the area and mean heat flux terms. Quantitatively, Nu_o and f_o change by −5.20% and +12.37% from G02 to G04 and by −7.63% and −13.10% from G02 to G06.

The reduction in pressure drop with increasing axial clearance is consistent with the spacing response reported by Wang et al. [27]. The thermal response depends additionally on how the tube length, area, and reference diameter change. The twisted helical study [7], for example, reported simultaneous increases of 33.4% in the Nusselt number and 57.6% in the friction factor relative to its untwisted reference. The conical coil study [8] similarly linked heat transfer gains to hydraulic penalties. These findings support joint thermal–hydraulic assessment, but the different fluids, passages, and definitions preclude a direct enhancement factor comparison.

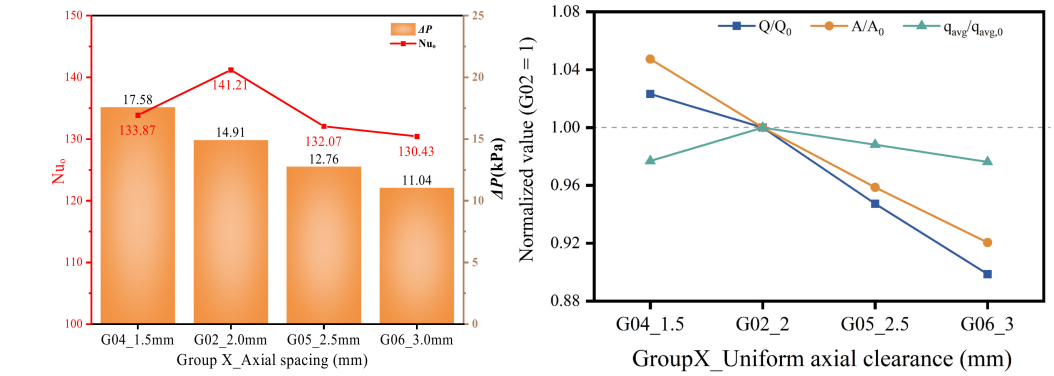


Figure 5. Effects of uniform axial tube spacing on heat transfer and flow resistance. (**a**) Nu_o and shell-side pressure drop; (**b**) heat duty, actual area, and mean heat flux relative to G02 (dashed line at unity); (**c**) velocity distributions in one half of a mid-length section of the shell-side molten salt.

5.3. Direction of Axial Clearance Allocation and Layer-Resolved Heat Transfer

G07, G02, and G08 share 8/8/8 mm tubes and 1/1 mm radial clearances but have axial clearances of 1.5/2/2.5, 2/2/2, and 2.5/2/1.5 mm, respectively (Figure 6). Changing the allocation alters the helical lead and actual layer area as well as the passage geometry.

Compared with G08, G07 has a 1.53% smaller area, yet its heat duty rises from 621.09 to 633.37 kW and the pressure drop falls from 15.162 to 14.601 kPa. The PEC increases from 0.8821 to 1.0122 (+14.74%), showing that the area alone does not explain the difference. Relative to G02, the changes are much smaller: +0.42% in heat duty, −2.07% in pressure drop, and +1.22% in the PEC. From G08 to G07, Nu_o increases by 15.75%, while f_o increases by 2.67%, despite the lower pressure drop. This difference arises because f_o also

contains the case-specific reference velocity and equivalent diameter; it is not a local wall skin friction coefficient.

From G08 to G07, the inner-, middle-, and outer-layer heat duties change by +3.80, −5.42, and +13.91 kW. The outer-layer gain dominates despite an 8.52% reduction in its area: its mean heat flux rises by 15.75% and heat duty by 5.88%. Its relative heat flux R_3 increases from 0.867 to 0.969, indicating an improved heat duty contribution relative to the area share.

A wider outer-layer axial clearance may alter tube-to-tube obstruction and the access of the hot fluid to the outer-layer walls. This interpretation is consistent with the integrated response, but R_3 combines convection and the local temperature difference. Neither R_3 nor the velocity contours measure the salt mass flow allocated to an individual radial passage.

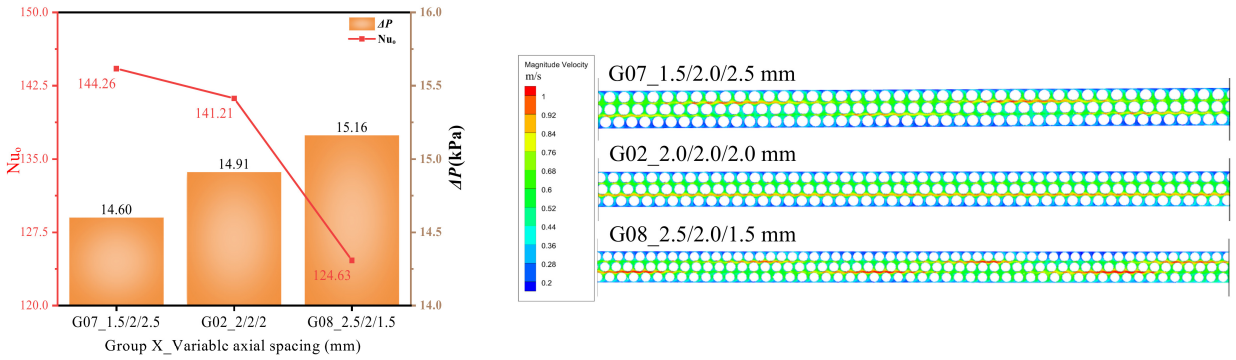


Figure 6. Effect of axial clearance allocation on shell-side performance. (**a**) Nu_o and pressure drop; (**b**) velocity distributions at the same section location.

5.4. Radial Clearance Allocation and Redistribution of Heat Transfer Contributions

G09, G10, G02, G11, and G12 share tube diameters and axial clearances, with the total radial clearance fixed at 2 mm. Their g_{12}/g_{23} values are 0.5/1.5, 0.75/1.25, 1/1, 1.25/0.75, and 1.5/0.5 mm. The outer clearance fraction χ in Equation (24) characterizes this allocation (Figure 7). G02 gives the highest heat duty and PEC among these cases.

Relative to G12, G09 increases the heat duty by 1.72% and the PEC by 12.39%, while reducing the pressure drop by 9.57%. The corresponding G10-versus-G11 changes are +0.75%, +5.78%, and −4.92%. Both mirrored pairs favor a larger outer clearance. Since both gaps change together, this is an allocation direction response rather than separate sensitivities to g_{12} and g_{23}. G09 also has an 11.13% higher Nu_o and a 3.32% lower f_o than G12, quantifying the different thermal and hydraulic responses to mirrored gap allocation.

The layer heat duties are 149.01/216.45/254.82 kW for G09 and 173.01/218.58/218.18 kW for G12. From G12 to G09, the outer layer gains 36.63 kW, offsetting a combined inner- and middle-layer loss of 26.13 kW. With a nearly unchanged outer-layer area, its 16.79% heat duty increase mainly reflects higher mean heat flux. The inner-layer heat duty falls by 13.87%, demonstrating redistribution rather than an improvement in every layer.

Changing radial allocation can affect passage resistance and local fluid temperatures. The nonuniform shell-side fields reported by Wang et al. [27] and the local thermal resistance analysis of Bi et al. [30] support examining such spatial differences. Here, Figure 8 places the layer integrals in their section-level context. The data identify an outer-layer gain for outward-biased allocation; they do not isolate a vortex, bypass, or radial mass-flow mechanism. Uniform allocation has the highest computed PEC in the present set.

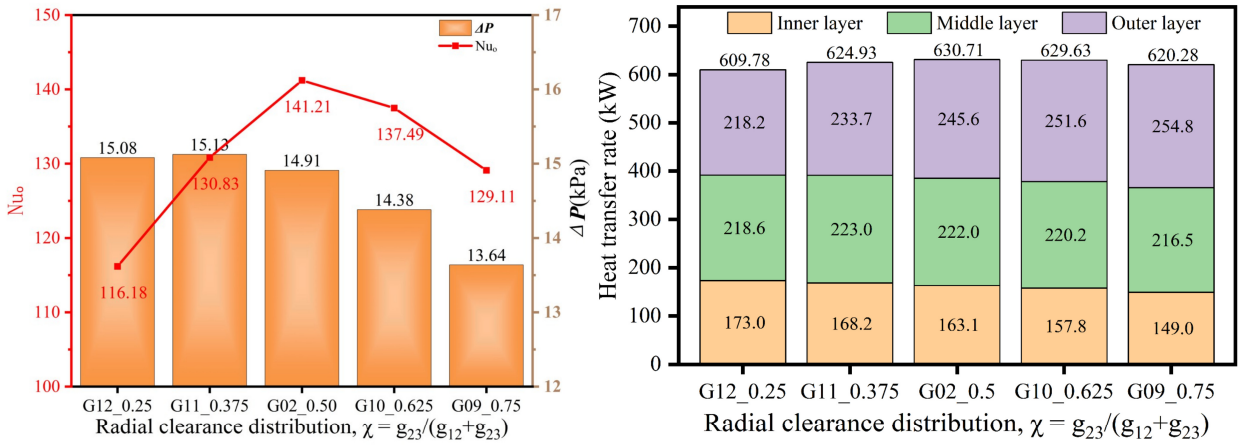


Figure 7. Radial clearance allocation at fixed total clearance. (**a**) Nu_o and Δp; (**b**) layer heat duties. Values following the case identifiers denote the dimensionless outer clearance fraction χ defined in Equation (24).

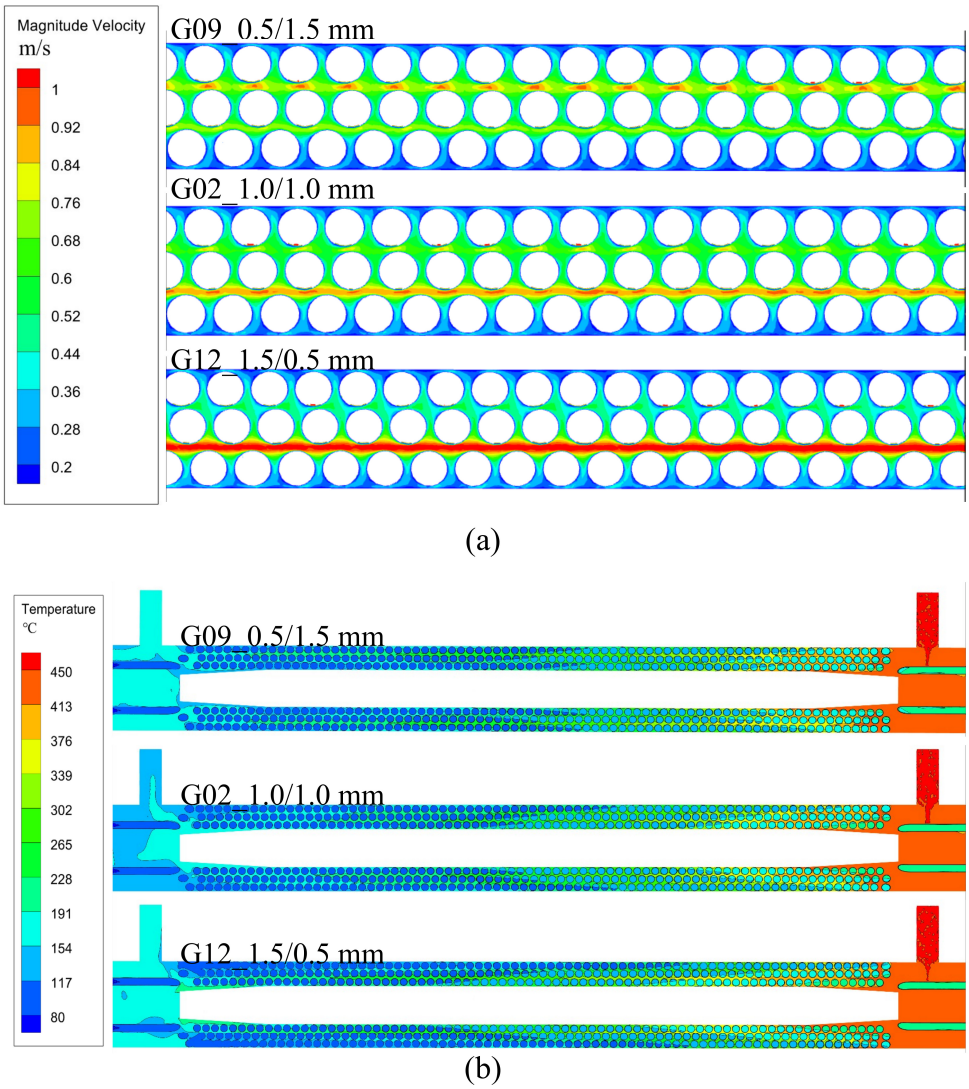


Figure 8. Shell-side velocity and overall temperature distributions for opposite radial clearance allocations. (**a**) Shell-side velocity distributions in G09, G02, and G12; (**b**) corresponding overall temperature distributions.

https://doi.org/10.3390/en19215337

5.5. Radial Tube Diameter Configuration at Fixed Interlayer Clearances

G02 and G13–G16 use 8/8/8, 7/8/9, 9/8/7, 7/9/8, and 8/7/9 mm tubes, respectively, with g_{12} = g_{23} = 1 mm and uniform 2 mm axial clearance. The tube diameter sum is 24 mm in every case. However, diameter placement among layers with different tube counts and lengths changes heat transfer and the tube-side flow areas. The comparison isolates the radial diameter arrangement from the total interlayer clearance, not from all associated geometric effects.

The five PEC values are 1.0000, 1.0118, 1.0001, 1.0225, and 1.0103. G15 has the highest computed value, with Q = 633.59 kW and Δp = 14.826 kPa: changes of +0.46%, −0.56%, and +2.25% relative to G02 in Q, Δp, and the PEC, respectively. These small differences do not establish a robust ranking without a case-specific uncertainty assessment. G14 has the highest duty in the set, 636.88 kW, while its PEC is almost unchanged from G02. The stronger result of Figure 9 is the redistribution of layer contributions.

Compared with G13, G14 increases the area by 2.20% and the heat duty by 1.27%, while decreasing the mean heat flux by 0.91% and the PEC by 1.16%. The inner-, middle-, and outer-layer heat duties change by −4.82, +3.62, and +9.22 kW. The outer-layer area falls by 5.25%, but its mean heat flux rises by 9.45%, giving a 3.70% greater heat duty. Thus, an outer-layer gain does not establish an overall advantage for an outward-decreasing diameter arrangement.

The redistribution may involve changes in bundle obstruction, winding curvature, tube-side flow area, and local temperature difference. Because an equal inlet mass flow is prescribed for every tube, these results describe the response under controlled branch flows rather than pressure-driven flow redistribution among branches. Gains in one layer can be offset by losses elsewhere and by flow resistance, leaving only a small difference in the overall PEC.

G03 and G17 provide a second comparison at a 1 mm total radial clearance, using 9/8/8 and 9/7/9 mm tubes. G17 has a 0.58% higher heat duty, 3.01% higher pressure drop, and 2.05% higher PEC. This also gives a small overall response compared with several clearance allocation adjustments.

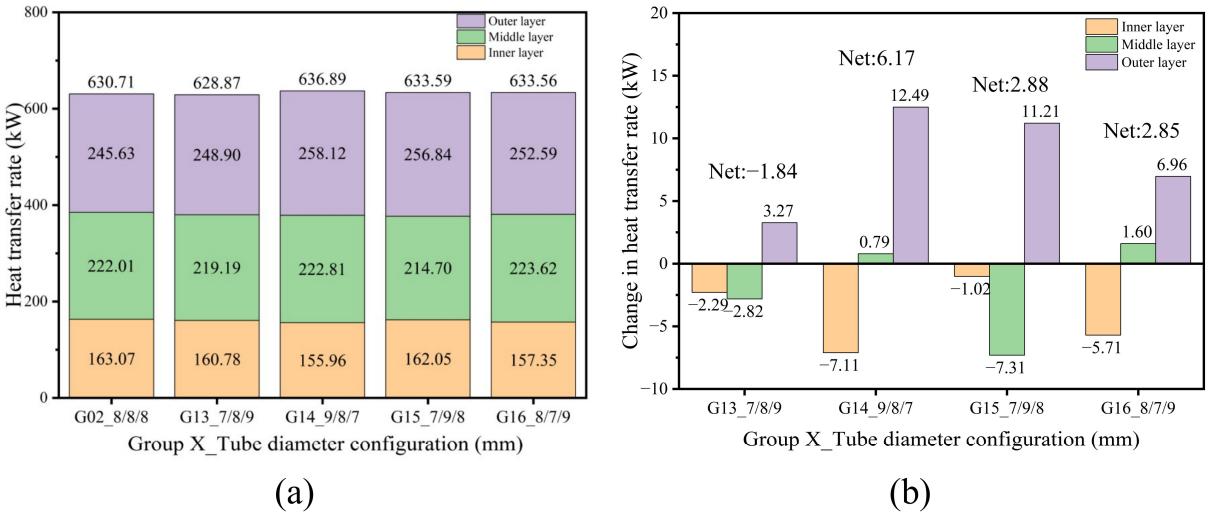


Figure 9. Effect of radial tube diameter configuration at fixed interlayer clearances. (**a**) Heat duties of the three layers; (**b**) changes in layer-resolved heat duty relative to G02.

5.6. Coupled Response of the Sum of the Tube Diameters and Radial Passages

Equation (2) couples the tube diameter sum and total radial clearance. G01, G19, G20, G02, and G03 use 7/7/7, 7/7/8, 7/8/8, 8/8/8, and 9/8/8 mm tubes, with total clearances of 5, 4, 3, 2, and 1 mm. This series follows a constrained design path; it cannot separately establish diameter and total clearance effects.

Along this path, the PEC is nonmonotonic: 1.1420, 0.9030, 0.9561, 1.0000, and 0.9542. G01 has a 5.83% lower heat duty, 54.37% lower pressure drop, and 14.20% higher PEC than G02. Its inferred h_o is 4071.08 W/(m²·K), below 5134.99 W/(m²·K) for G02. Its advantage is therefore low resistance with a modest heat duty reduction, not a higher heat transfer coefficient (Figure 10).

From G01 to G19, the area rises by 2.03%, but the heat duty falls by 3.10%; the pressure drop rises by 19.47% and the PEC falls by 20.93%. The inner- and middle-layer gains of 5.54 and 15.49 kW do not offset the outer-layer loss of 39.43 kW. The outer tube diameter and both radial clearances change together, so the loss cannot be assigned to either variable alone.

The heat duty and pressure drop increase from G19 through G20 to G02. The further change to G03 gives only a 2.49% larger heat duty but a 43.32% larger pressure drop, reducing the PEC to 0.9542. Narrower passages and a larger diameter sum can therefore increase the thermal capacity with a disproportionate resistance penalty along this design path.

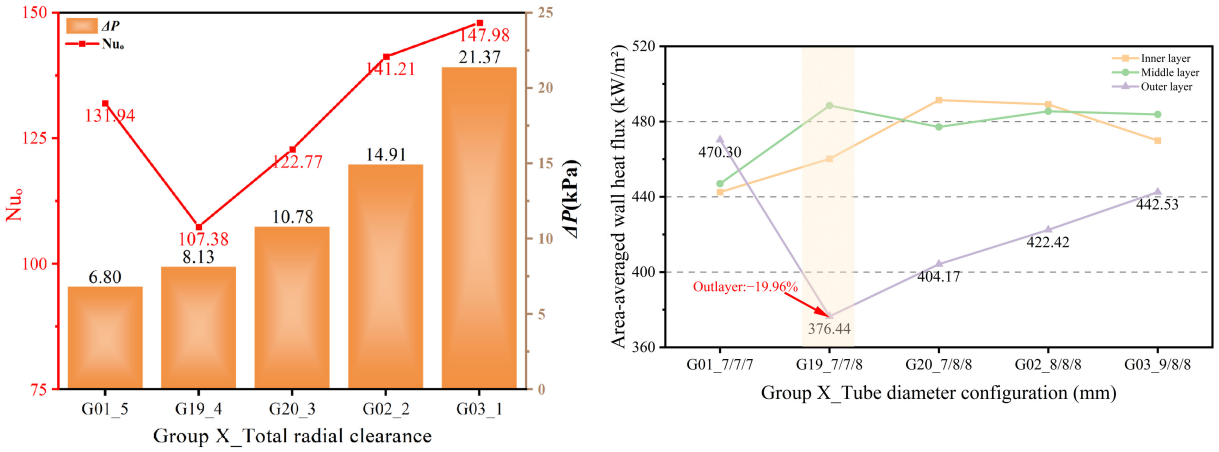


Figure 10. Coupled response of tube diameters and total interlayer clearance within a constrained radial space. (**a**) Nu_o and shell-side pressure drop; (**b**) area-averaged heat flux over the outer tube walls of each layer.

5.7. Combined Adjustments and Quantitative Decomposition of Heat Duty Changes

G21 and G22 reduce the uniform axial clearance of G01 and G14 from 2.0 to 1.5 mm without changing the tube diameters or radial clearances. Together with G02–G04, these pairs test the same adjustment in three structural settings (Figure 11), followed by the decomposition in Section 3.5.

From G01 to G21, the area increases by 6.84%, while the heat duty falls from 593.97 to 571.52 kW. The pressure drop rises from 6.804 to 7.705 kPa and the PEC falls from 1.1420 to 0.8528. The inner- and middle-layer gains of 6.22 and 25.18 kW are outweighed by an outer-layer loss of 53.85 kW. Despite a 9.67% increase in the maximum shell-side velocity, the total heat duty decreases by 22.45 kW.

From G14 to G22, the area rises by 5.19%, heat duty by 2.89%, and pressure drop by 17.67%, while the PEC falls by 5.73%. All layers gain heat duty, but the overall gain is smaller than the area increase. G22 reaches 655.26 kW, the largest duty among the cases examined, with an 18.73% greater pressure drop than G02.

The three adjustments change the heat duty by +2.32%, −3.78%, and +2.89%, respectively, while reducing the PEC in every pair. The response therefore depends on the combined tube diameter and radial passage setting; these comparisons do not separate their individual interactions with axial spacing.

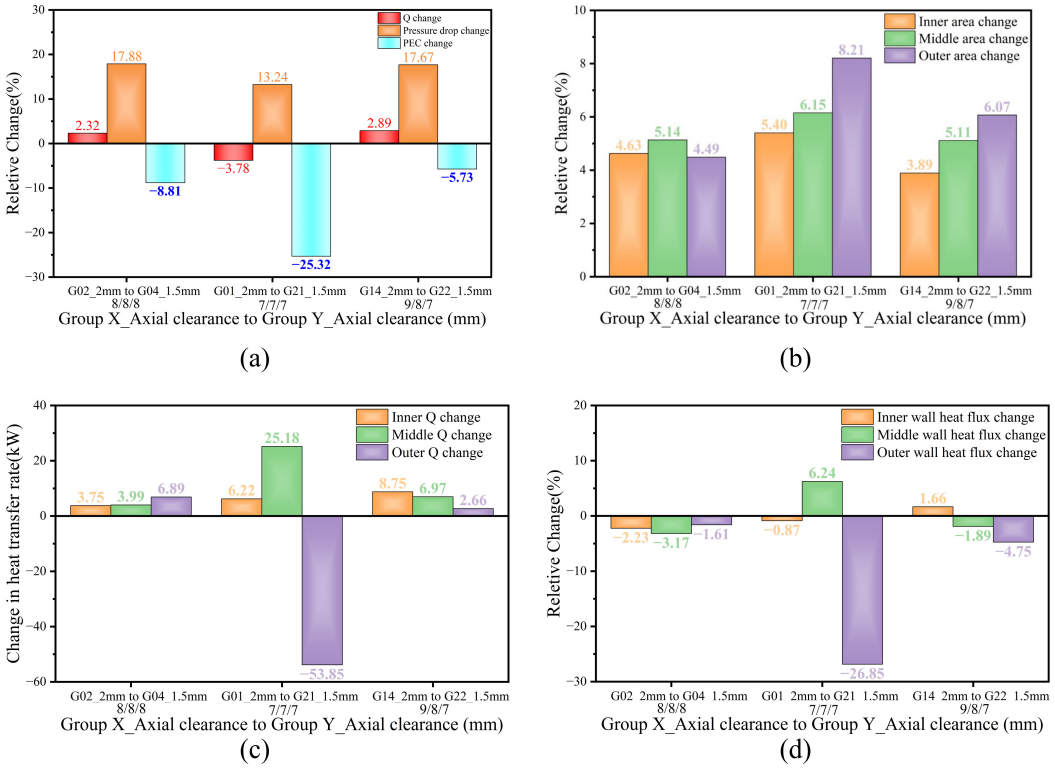


Figure 11. Effects of axial clearance adjustment for different tube diameter configurations. (**a**) Relative changes in total Q, Δp, and PEC; (**b**) changes in the actual heat transfer area of each layer; (**c**) gains and losses in layer-resolved heat duty; (**d**) changes in the mean heat flux of each layer.

Equations (25)–(28) and Figure 12 give total area terms of +29.62, +38.31, and +32.70 kW for G02–G04, G01–G21, and G14–G22. The corresponding mean heat flux terms are −14.99, −60.76, and −14.31 kW, giving net changes of +14.63, −22.45, and +18.39 kW. Table 7 supplies the underlying layer duties and mean fluxes. The sign difference for G01–G21 results from its larger negative heat flux term in this exact decomposition.

Table 7. Layer heat duties and area-weighted mean outer-wall heat fluxes for the three axial clearance comparisons.

Case	Inner Q (kW)	Middle Q (kW)	Outer Q (kW)	Inner Mean Flux (kW/m²)	Middle Mean Flux (kW/m²)	Outer Mean Flux (kW/m²)
G02	163.07	222.01	245.63	489.14	485.46	422.42
G04	166.81	226.01	252.52	478.25	470.05	415.62
G01	138.65	197.02	258.30	442.49	446.96	470.30
G21	144.87	222.19	204.45	438.65	474.86	344.03
G14	155.96	222.81	258.12	444.21	475.02	460.67
G22	164.71	229.78	260.77	451.57	466.06	438.79

Note: Each pair follows a 2.0-to-1.5 mm axial clearance adjustment. Heat duties and mean fluxes use the same layer wall surfaces and actual areas. They describe thermal contributions, not shell-side mass-flow fractions.

In G01–G21, the outer layer has an area term of +18.35 kW and a mean heat flux term of −72.20 kW, yielding the net loss of 53.85 kW. In G02–G04, every negative heat flux term is smaller than its corresponding area term. In G14–G22, both inner-layer terms are positive, whereas the middle and outer layers combine positive area terms with negative heat flux terms. These differences locate the source of the net response without treating the terms as independent geometric effects.

For G01–G21, Equation (29) combines a 14.73% fall in U_o, a 6.84% area increase, and a 5.62% increase in the logarithmic mean temperature difference into a 3.78% heat duty decrease. Their logarithmic contributions are −0.15937, +0.06613, and +0.05470, summing to −0.03853 within rounding. The larger terminal driving force does not offset the lower inferred U_o; this is a consistency check using the same overall results.

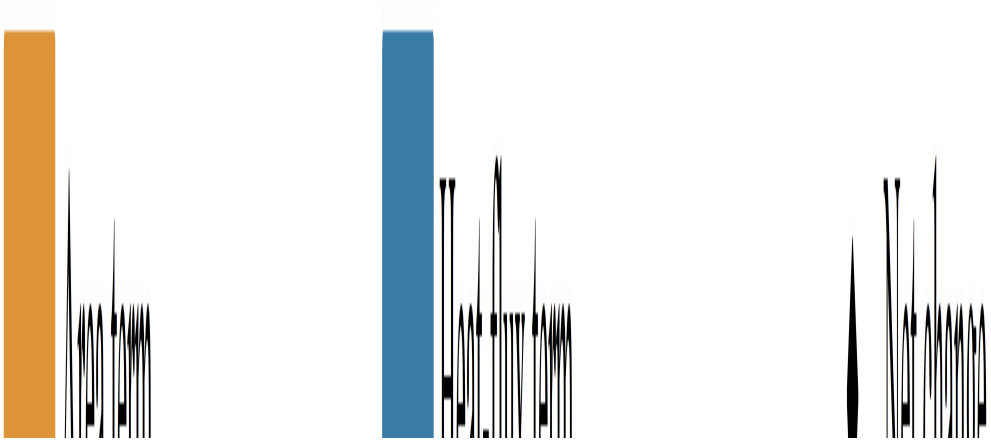


Figure 12. Layer-resolved decomposition of heat duty changes: (**a**) G02–G04; (**b**) G01–G21; (**c**) G14–G22. Orange and blue bars give area and mean heat flux terms; black diamonds give their sums. The terms are a symmetric mathematical decomposition, not independent single-variable effects. The horizontal line at zero separates increases from decreases in layer heat duty.

Figure 13 shows the wall heat flux distribution for G01 and G21 on a common scale. Their outer-layer mean heat flux falls from 470.30 to 344.03 kW/m² (−26.85%), whereas the inner- and middle-layer values change from 442.49 to 438.65 and from 446.96 to 474.86 kW/m² (Table 7). These integrals quantify the spatial contrast. Passage contraction, wall access, and local temperatures may contribute, but the available contours do not independently resolve their causal contributions or quantify interlayer salt flow fractions.

Thus, an increased area does not guarantee increased mean heat flux in each layer. In G21, the outer-layer loss outweighs the gains elsewhere, whereas G04 and G22 retain positive total heat duty changes. This is a coupled response to axial adjustment within each existing diameter and radial passage configuration.

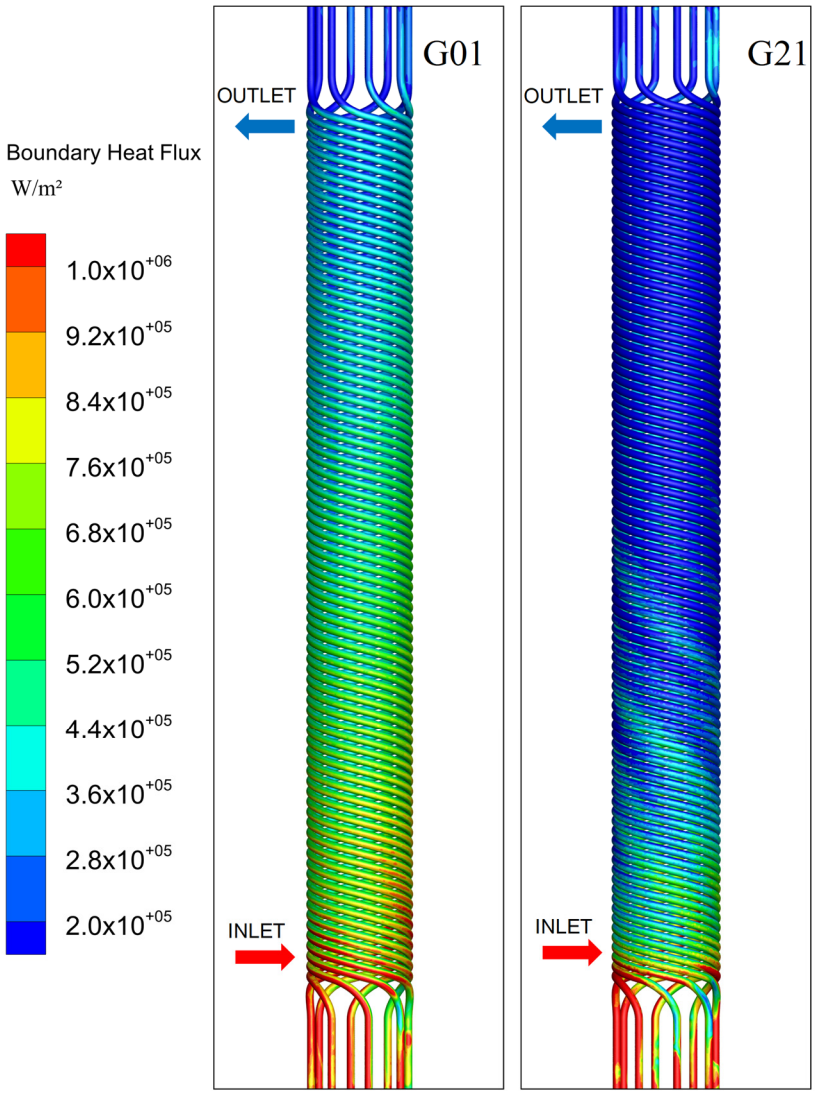


Figure 13. Outer tube wall heat flux distributions of G01 and G21. G01 and G21 are shown on the left and right, respectively, using the same color scale. Quantitative comparisons of layer-resolved heat duty and mean heat flux use statistics obtained with consistent surface selection.

5.8. Overall Comparison and Structural Selection

Figure 14 compares all 22 configurations. G01 has the highest computed PEC (1.1420) and lowest pressure drop (6.804 kPa), with Q = 593.97 kW. G22 has the highest Q, 655.26 kW, with Δp = 17.703 kPa and a PEC = 0.9428. Table 8 distinguishes their objectives. At the common salt flow of 3 m³/h, the nominal shell-side hydraulic power is 5.67 W for G01, 12.43 W for G02, and 14.75 W for G22. Thus, G01 reduces the shell-side hydraulic requirement by 54.37% while sacrificing 5.83% of duty; G22 adds 3.89% duty with 18.73% more hydraulic power.

Table 8. Heat duty and hydraulic requirements of the reference and two design candidates at salt flow 3 m³/h.

Case	Heat Duty (kW)	Pressure Drop (kPa)	Nominal Shell Hydraulic Power (W)	PEC
G01	593.97	6.804	5.67	1.1420
G02	630.71	14.910	12.43	1.0000
G22	655.26	17.703	14.75	0.9428

Note: Hydraulic power is the nominal fluid power across the modeled shell-side domain. Water-side losses, external piping, and pump efficiency are excluded; the values are not total plant electricity consumption.

These are alternative design priorities, not a single universal optimum. G01 is a candidate where a lower hydraulic demand is valuable and its duty is sufficient; G22 is a candidate for higher duty at the same prescribed flow. Their total pumping energy or economic advantage cannot be determined without water-side pressure losses, external-loop losses, pump efficiencies, and the required load. G07 and G15 show much smaller gains over G02, which are treated as provisional calculated differences.

The maximum-to-minimum PEC spans are 0.1676 for radial clearance allocation, 0.0881 for uniform axial clearance, and 0.0225 for diameter arrangement at fixed clearances. This ranks the response magnitudes only over the selected ranges and constraints. It is neither a universal sensitivity ranking nor the separation of coupled diameter sum and total clearance effects.

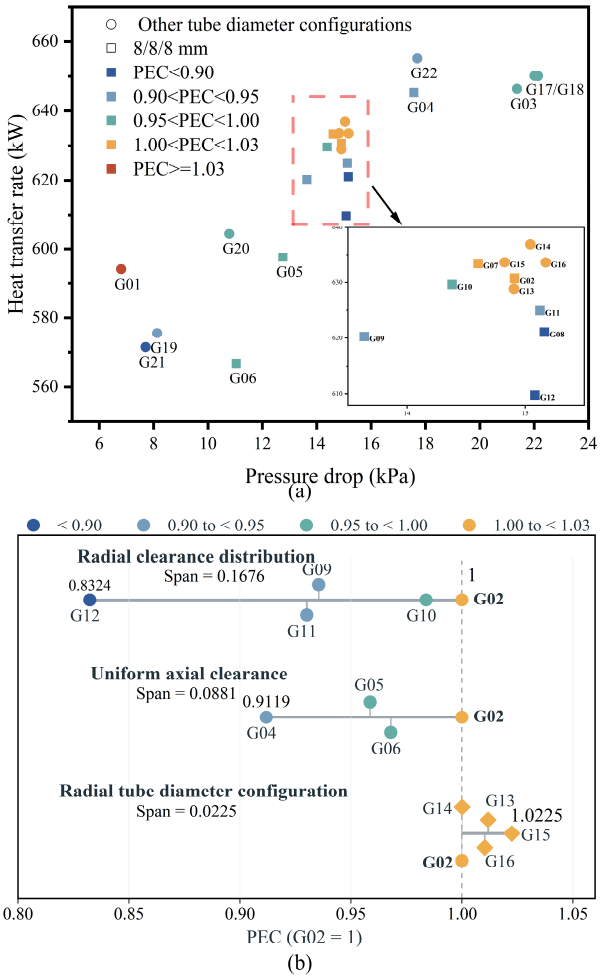


Figure 14. Heat duty–pressure-drop trade-off for all configurations. (**a**) Q versus Δp, colored by PEC; (**b**) PEC ranges within three comparison sets. The spans represent the tested parameter ranges, not universal sensitivities. The dashed box in (**a**) identifies the region enlarged in the inset. The vertical dashed line in (**b**) marks the G02 reference (PEC = 1).

5.9. Exploratory Comparison of Flow Rate Responses

A supplementary SWHE dataset is compared with simulations of the segmental baffle geometry specified in Table 1 of Chen et al. [32], all performed by the present research

group at salt and water inlet temperatures of 450 and 80 °C. This SWHE configuration is separate from the 22-case structural series. The datasets retain their respective index normalizations, and the baffle model has not been independently validated; the comparison is therefore exploratory rather than a quantitative measure of cross-configuration enhancement.

At a fixed salt flow rate of 3.0 m³/h, increasing water flow from 3.8 to 5.6 m³/h raises the reported index J from 120.80 to 132.97 for the supplementary SWHE, while the baffle value decreases from 70.72 to 65.68 (Figure 15a). The different trend directions suggest configuration-dependent responses to cold-side flow. Changes in tube-side thermal resistance and the thermal capacity rate may contribute, alongside the temperature dependence of the post-processed quantities.

At a fixed water flow rate of 4.4 m³/h, increasing salt flow from 2.1 to 4.2 m³/h raises J from 92.91 to 171.20 for the SWHE and from 53.19 to 86.65 for the baffle model, or by 84.27% and 62.92% within their respective datasets (Figure 15b). Both series indicate increasing index values with hot-side flow. These trends supplement the fixed-inlet structural analysis without establishing an equal-pumping-power advantage.

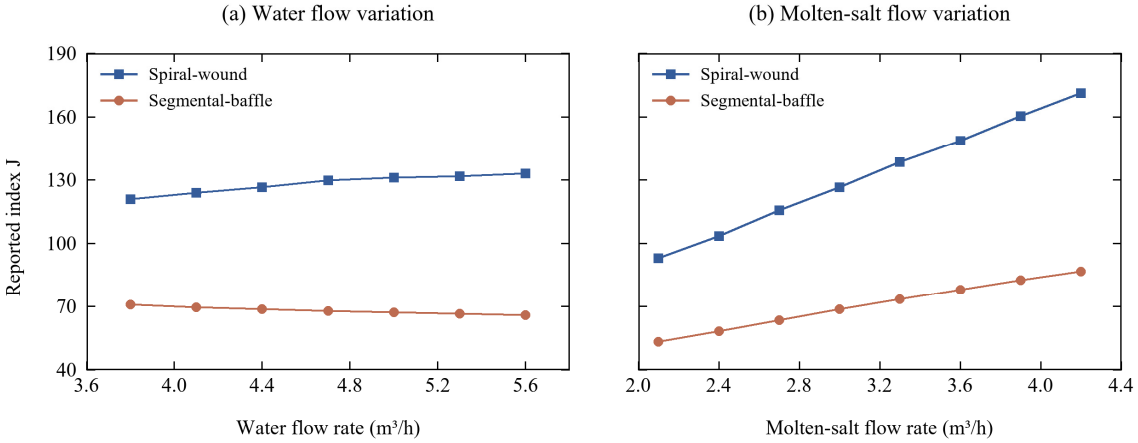


Figure 15. Exploratory flow rate responses of the supplementary SWHE and segmental baffle datasets. (**a**) Water flow variation at salt flow 3.0 m³/h; (**b**) salt flow variation at water flow 4.4 m³/h. Inlet temperatures are 450/80 °C. Each series retains its own index normalization.

5.10. Local Correlations for the Uniform-Diameter Subset

The ten-case subset in Section 3.6 isolates spacing adjustments within the 8/8/8 mm tube family. Equation (31) uses the G02 reference values $Nu_{o,0}$ = 141.2088 and $f_{o,0}$ = 0.0252309. Table 9 gives the fitted coefficients; Table 10 reports the fit and leave-one-out errors. The same functional form is used for both responses, and no case is removed on the basis of its prediction error.

Table 9. Coefficients of the local geometric response correlation in Equation (31).

Response y	c_0	c_1	c_2	c_3	c_4
Nu_o	0.95967	−0.05647	0.13901	0.09212	−0.35214
f_o	1.01429	−0.32370	0.02672	−0.03338	−0.27660

Table 10. Descriptive fit and leave-one-out prediction errors for the ten-case subset.

Response	Fit R^2	Fit Mean Error (%)	Fit Max. Error (%)	LOO Mean Error (%)	LOO Max. Error (%)
Nu_o	0.9012	1.36	4.03	2.75	4.90
f_o	0.9510	1.12	2.54	2.57	6.03

The mean errors in Table 10 are mean absolute relative deviations, with each CFD-derived value as the denominator. The fitted R^2 values are 0.9012 for Nu_o and 0.9510 for f_o. Leaving out one case at a time increases the mean deviations to 2.75% and 2.57%, respectively, with maxima of 4.90% and 6.03%. These internal checks support a compact representation of the sampled responses, but ten cases and five coefficients provide limited evidence for prediction beyond these paths. The fit does not replace the original CFD results for resolving small differences or selecting a new optimum.

For context, Mostafazade Abolmaali and Afshin [21] used 64 geometries to develop multivariate shell-side correlations incorporating the layer count and dimensionless longitudinal and radial pitches, reporting mean deviations of 5.4% for Nu and 7.0% for the friction factor. The present correlation instead represents local spacing responses at fixed inlet conditions and retains the apparatus-level f_o definition in Equation (19). Its smaller fit deviations cannot establish greater predictive accuracy because the datasets, parameter ranges, and evaluation procedures differ. The comparison is therefore performed at the level of geometric dependence and applicability, rather than by applying incompatible correlations directly to the present values.

The positive ζ and ψ coefficients in the Nu_o response describe the tendency toward higher values for outward-biased axial and radial allocations within the sampled families. The negative ψ^2 term captures the loss associated with sufficiently uneven radial allocation. These are aggregate configuration responses, including changes in area, winding position, and mean properties. Simultaneous axial and radial changes were not sampled, so interactions are unidentifiable and the correlation must not be used to predict an unsimulated combined adjustment.

6. Conclusions

The conclusions apply to the 22 numerical configurations with a 96 mm shell, 42 mm core, three layers containing 4/6/8 tubes, and prescribed equal mass flow among individual tube inlets. The tube diameters are 7–9 mm, the nominal axial clearances are 1.5–3 mm, and the total interlayer clearance is 1–5 mm under the coupled constraint in Equation (2). Structural comparisons use salt/water inlet temperatures of 450/80 °C and nominal flow rates of 3/5 m^3/h.

(1) Axial clearance effects depend on the diameter configuration. Reducing the clearance from 2.0 to 1.5 mm changes the heat duty by +2.32%, −3.78%, and +2.89% for G02–G04, G01–G21, and G14–G22, respectively. For G01–G21, the +38.31 kW area term is outweighed by the −60.76 kW mean heat flux term, with the net loss concentrated in the outer layer.

(2) With the total radial clearance fixed at 2 mm, uniform allocation gives the highest sampled PEC. Among mirrored nonuniform allocations, G09 has an 11.13% higher Nu_o, 9.57% lower pressure drop, and 12.39% higher PEC than G12. Its 36.63 kW outer-layer gain offsets a combined 26.13 kW loss from the inner and middle layers, demonstrating redistribution across layers.

(3) Diameter arrangement at fixed clearances produces a PEC span of only 0.0225. The selected PEC spans for radial allocation and uniform axial clearance are larger, at 0.1676 and 0.0881. These values rank the tested response ranges; they do not establish universal parameter sensitivities or separate coupled diameter and clearance effects.

(4) G01 and G22 meet different design objectives. Relative to G02, G01 reduces the nominal shell-side hydraulic power by 54.37% with a 5.83% duty reduction and a 14.20% PEC increase. G22 gives the highest duty, 655.26 kW, with 18.73% more shell-side hydraulic power. These results support choosing a structure against a specified heat load and allowable pressure loss.

(5) For G02 and G04–G12, local geometric response correlations give leave-one-out mean deviations of 2.75% for Nu_o and 2.57% for f_o. They summarize the sampled spacing paths at fixed inlet conditions and are not general Reynolds number correlations or independently validated predictors.

(6) The supplementary flow rate comparison shows configuration-dependent responses to water flow and increasing performance indices with salt flow. It provides an exploratory operating condition comparison rather than a cross-configuration enhancement factor.

Direct molten salt experiments and operating condition sweeps are priorities for testing these candidate designs. Further assessments should quantify the property and boundary input sensitivities, buoyancy, transient flow, wall heat spreading, turbulence model dependence, and pressure-driven branch maldistribution. The present steady, constant-water-property calculations support structural screening; small differences and absolute performance predictions require additional evidence.

Author Contributions: Conceptualization, X.F., Z.L. and Z.Z.; methodology, X.H., J.C., X.F. and Z.Z.; validation, X.H.; formal analysis, X.H. and J.C.; investigation, X.H., J.C. and T.H.; resources, X.F. and Z.L.; writing—original draft, X.H.; writing—review and editing, X.H., J.C., T.H. and Z.Z.; visualization, J.C. and T.H.; supervision, X.F. and Z.L.; project administration, Z.Z.; funding acquisition, Z.L. and Z.Z. All authors have read and agreed to the published version of the manuscript.

Funding: This work was supported by the National Key R&D Program of China (No. 2022YFB2405204).

Data Availability Statement: Data supporting the findings are available from the corresponding author upon reasonable request.

Acknowledgments: During the preparation of this manuscript, the authors used ChatGPT (GPT-6.0 Astra, OpenAI) to assist with English translation, proofreading, and language polishing. The authors reviewed and edited the output and take full responsibility for the content of this publication.

Conflicts of Interest: The authors declare no conflicts of interest.

Nomenclature

Symbol	Description
Latin symbols	
A_i, A_o	Total inner and outer tube wall heat transfer areas, respectively [m²]
A_j	Actual outer tube wall heat transfer area of layer j [m²]
$A_{f,w}$	Total tube-side flow cross-sectional area [m²]
$C_{A,j}$, $C_{q,j}$	Area change and mean heat flux change contributions to the heat duty change of layer j, respectively [W]
$C_{r,j}$	Layer-specific curvature correction factor for tube-side heat transfer [–]
C_1, C_2, $C_{1\varepsilon}$, $C_{3\varepsilon}$	Coefficients in the realizable k–ε turbulence model [–]
c_p	Specific heat capacity at constant pressure [J·kg^{-1}·K^{-1}]
$D_{c,j}$, $R_{c,j}$	Winding center diameter and radius of layer j, respectively [m]
D_e	Shell-side equivalent diameter defined as $4V_s/A_o$ [m]
d_j, $d_{i,j}$	Tube outer and inner diameters in layer j, respectively [m]
$\bar{d_o}$, $\bar{d_i}$	Tube count-weighted mean outer and inner diameters, respectively [m]
F_i	Additional body force component per unit volume [N·m^{-3}]
f_i	Tube-side friction factor used in the base Nusselt number correlation [–]
f_o	Shell-side flow resistance metric based on the maximum shell-side velocity [–]
G_k, G_b	Turbulent kinetic energy production by mean velocity gradients and buoyancy, respectively [W·m^{-3}]
$g_{a,j}$	Nominal axial clearance between tubes in layer j [m]

g_{12}, g_{23}	Radial net clearances between the inner/middle and middle/outer tube layer envelopes, respectively [m]
g_i	Gravitational acceleration component [m·s^{-2}]
h	Specific enthalpy in the energy equation [J·kg^{-1}]
$h_{i,j}$	Estimated internal heat transfer coefficient of layer j [W·m^{-2}·K^{-1}]
h_i, h_o	Equivalent tube-side and shell-side heat transfer coefficients, respectively [W·m^{-2}·K^{-1}]
J	Overall performance metric, $Nu_o/f_o^{1/3}$ [–]
k	Turbulent kinetic energy [m^2·s^{-2}]
L_s	Shell-side axial characteristic length [m]
$\dot{m}$	Mass flow rate [kg·s^{-1}]
N_j	Number of tubes in layer j [–]
Nu_b, Nu_o	Base tube-side and shell-side Nusselt numbers, respectively [–]
P_j	Lead of the multistart helix in layer j [m]
p, Δp	Static pressure and shell-side inlet-to-outlet pressure drop, respectively [Pa]
PEC	Performance evaluation criterion normalized to G02, J/J_0 [–]
Pr_w, Re_w	Equivalent water-side Prandtl and Reynolds numbers, respectively [–]
Q, Q_j	Total heat duty and heat duty of layer j, respectively [W]
ΔQ, ΔQ_j	Changes in total and layer-resolved heat duty, respectively [W]
q''_j, $\bar{q}''_j$	Local and area-weighted mean outer tube wall heat fluxes of layer j, respectively [W·m^{-2}]
R_j	Mean wall heat flux of layer j relative to the overall mean, $\eta_{Q,j}/\eta_{A,j}$ [–]
$R''_{wall,o}$	Equivalent area-specific tube wall thermal resistance based on outer area [m^2·K·W^{-1}]
R^2	Coefficient of determination [–]
S	Mean strain rate magnitude [s^{-1}]
S_h	Volumetric energy source term [W·m^{-3}]
T, T_m	Temperature and mean reference temperature for property evaluation, respectively [K or °C, as specified]
ΔT_1, ΔT_2, ΔT_{lm}	Terminal temperature differences and logarithmic mean temperature difference [K]
t	Time [s]
U_o	Overall heat transfer coefficient based on the outer tube wall area [W·m^{-2}·K^{-1}]
u_i, u_j	Cartesian velocity components [m·s^{-1}]
u_w, u_{max}	Equivalent mean tube-side velocity and maximum shell-side fluid velocity, respectively [m·s^{-1}]
V_s	Shell-side fluid domain volume [m^3]
$\dot{V}$	Volumetric flow rate [m^3·s^{-1}]
x_i, x_j	Cartesian coordinates [m]
Y_M	Compressibility-related dilatation contribution in the turbulent kinetic energy equation [W·m^{-3}]
c_0–c_4	Fitted coefficients of the local geometric response correlation [–]
$\bar{g}_a$, $g_{a,0}$	Arithmetic mean axial clearance and reference clearance of G02, respectively [m]
y, y_0	Local correlation response (Nu_o or f_o) and its G02 reference value [–]
Greek symbols	
ε	Dissipation rate of turbulent kinetic energy [m^2·s^{-3}]
$\eta_{Q,j}$, $\eta_{A,j}$	Heat duty contribution and outer area fraction of layer j, respectively [–]
λ, λ_{eff}	Thermal conductivity and effective thermal conductivity, respectively [W·m^{-1}·K^{-1}]
μ, μ_t	Dynamic viscosity and turbulent viscosity, respectively [Pa·s]
ν	Kinematic viscosity [m^2·s^{-1}]
ρ	Fluid density [kg·m^{-1}]
σ_k, σ_ε	Turbulent Prandtl numbers for k and ε, respectively [–]
τ_{ij}	Stress tensor component [Pa]
φ	Temperature-dependent thermophysical property; units depend on the property

χ	Fraction of total interlayer radial clearance assigned to the outer gap, $g_{23}/(g_{12} + g_{23})$ [–]
ξ, ζ, ψ	Dimensionless mean axial clearance change, axial allocation direction, and radial allocation direction, respectively [–]
Subscripts and indices	
0	Reference configuration G02
a, *b*	States before and after a structural modification; also the lower and upper temperature endpoints in property interpolation (Equation (4))
b	Base value in Nu_b; state after an adjustment
c	Winding center
eff	Effective
est	Estimate based on mean fluid properties and inlet/outlet conditions
i, *o*	Inner/tube-side and outer/shell-side quantities, respectively
in, *out*	Inlet and outlet, respectively
j	Tube layer index (1: inner; 2: middle; 3: outer); Cartesian summation index in the governing equations
i	Cartesian summation index in the governing equations
k	Fluid index (s or w) in the property and heat duty equations; k-transport quantity in turbulence model subscripts
lm	Logarithmic mean
m	Mean reference temperature
max	Maximum
s, *w*	Molten salt and water, respectively
t	Turbulent
wall	Tube wall
Abbreviations	
LOO	Leave-one-out cross-validation
SWHE	Spiral-wound heat exchanger
PEC	Performance evaluation criterion

References

1. Liu, X.; Zhong, Y.; Li, J.; Wang, H.; Wang, M. A Review of High-Temperature Molten Salt for Third-Generation Concentrating Solar Power. *Energy Sci. Eng.* **2025**, *13*, 456–474. https://doi.org/10.1002/ese3.2029.
2. Zheng, C.; Cheng, K.; Han, D. High-Temperature Molten Salt Heat Exchanger Technology: Research Advances, Challenges, and Future Perspectives. *Energies* **2025**, *18*, 3195. https://doi.org/10.3390/en18123195.
3. Mahmoudinezhad, S.; Sadi, M.; Ghiasirad, H.; Arabkoohsar, A. A comprehensive review on the current technologies and recent developments in high-temperature heat exchangers. *Renew. Sustain. Energy Rev.* **2023**, *183*, 113467. https://doi.org/10.1016/j.rser.2023.113467.
4. Hood, K.; Walsh, M.; Zolan, A.; Jackson, G.; Newman, A. Characterizing and improving the performance of molten-salt-steam heat exchangers in concentrating solar power plants. *Energy Convers. Manag.* **2024**, *315*, 118721. https://doi.org/10.1016/j.enconman.2024.118721.
5. Huang, T.; Huang, X.; Fang, X.; Ling, Z.; Zhang, Z. Research Progress on Thermophysical Properties and Convection Heat Transfer Enhancement of Molten Salts. *Energies* **2026**, *19*, 1230. https://doi.org/10.3390/en19051230.
6. Huang, T.; Chen, J.; Ling, Z.; Fang, X.; Zhang, C.; Zhang, Z. Numerical Investigation on the Thermal-Hydraulic Performance of Molten Salt in Internal Helically Finned Tubes. *Energies* **2026**, *19*, 3599. https://doi.org/10.3390/en19153599.
7. Abdelmagied, M. Determining of the thermo-hydraulic characteristics and exergy analysis of a triple helical tube with inner twisted tube. *Chem. Eng. Process. Process Intensif.* **2024**, *204*, 109922. https://doi.org/10.1016/j.cep.2024.109922.
8. Abdelmagied, M.M. Experimental investigation of the thermofluid performance and exergy analysis of a shell and twisted conical coil. *Appl. Therm. Eng.* **2026**, *299*, 131077. https://doi.org/10.1016/j.applthermaleng.2026.131077.
9. Qian, J.; Kong, Q.-L.; Zhang, H.-W.; Zhu, Z.-H.; Huang, W.-G.; Li, W.-H. Experimental study for shell-and-tube molten salt heat exchangers. *Appl. Therm. Eng.* **2017**, *124*, 616–623. https://doi.org/10.1016/j.applthermaleng.2017.06.005.
10. Qiu, Y.; Li, M.-J.; Wang, W.-Q.; Du, B.-C.; Wang, K. An experimental study on the heat transfer performance of a prototype molten-salt rod baffle heat exchanger for concentrated solar power. *Energy* **2018**, *156*, 63–72. https://doi.org/10.1016/j.energy.2018.05.040.

11. Xie, Q.; Liang, C.; Fu, Q.; Wang, X.; Liu, Y. Numerical investigation on heat transfer performance of molten salt in shell and tube heat exchangers with circularly perforated baffles. *J. Renew. Sustain. Energy* **2022**, *14*, 023703. https://doi.org/10.1063/5.0083647.
12. Khaliquzzama, M.A.; Masuri, S.U.; Saidur, R.; Hairuddin, A.A.; Tahir, S.M.; Malek, N.A. Heat transfer analysis of molten salt nitrates inside shell and tube heat exchanger with small round holed segmental baffles for concentrated solar power. *Int. J. Heat Fluid Flow* **2025**, *116*, 109916. https://doi.org/10.1016/j.ijheatfluidflow.2025.109916.
13. Chen, J.; Ling, Z.; Fang, X.; Wu, Y.; Zhang, Z. Numerical simulation on the flow and heat transfer characteristics of molten salt nanofluid in the shell-side of helical baffle heat exchangers with elliptic tubes and circular tubes. *Sol. Energy Mater. Sol. Cells* **2025**, *290*, 113733. https://doi.org/10.1016/j.solmat.2025.113733.
14. Weikl, M.C.; Braun, K.; Weiss, J. Coil-wound Heat Exchangers for Molten Salt Applications. *Energy Procedia* **2014**, *49*, 1054–1060. https://doi.org/10.1016/j.egypro.2014.03.113.
15. Pardillos-Pobo, D.; González-Gómez, P.A.; Laporte-Azcué, M.; Cholette, M.E.; Santana, D. Design of coil-wound heat exchangers for molten chloride salt TES in CSP with sodium receiver and sCO_2 cycle. *J. Energy Storage* **2025**, *128*, 117210. https://doi.org/10.1016/j.est.2025.117210.
16. Dong, X.; Wu, Y.; Zhang, C.; Lu, Y.; Ma, C. Experimental and numerical study on heat transfer and flow characteristics of molten salt nanofluids in spiral-wound tube heat exchanger. *Int. J. Therm. Sci.* **2023**, *191*, 108343. https://doi.org/10.1016/j.ijthermalsci.2023.108343.
17. Neeraas, B.O.; Fredheim, A.O.; Aunan, B. Experimental shell-side heat transfer and pressure drop in gas flow for spiral-wound LNG heat exchanger. *Int. J. Heat Mass Transf.* **2004**, *47*, 353–361. https://doi.org/10.1016/s0017-9310(03)00400-9.
18. Lu, X.; Du, X.; Zeng, M.; Zhang, S.; Wang, Q. Shell-side thermal-hydraulic performances of multilayer spiral-wound heat exchangers under different wall thermal boundary conditions. *Appl. Therm. Eng.* **2014**, *70*, 1216–1227. https://doi.org/10.1016/j.applthermaleng.2014.02.053.
19. Lu, X.; Zhang, G.; Chen, Y.-T.; Wang, Q.; Zeng, M. Effect of geometrical parameters on flow and heat transfer performances in multi-stream spiral-wound heat exchangers. *Appl. Therm. Eng.* **2015**, *89*, 1104–1116. https://doi.org/10.1016/j.applthermaleng.2015.04.084.
20. Wu, J.; Tian, Q.; Sun, X.; Zhao, J.; Wang, L.; Peng, X.; Liao, X. Numerical simulation and experimental research on the comprehensive performance of the shell side of the spiral wound heat exchanger. *Appl. Therm. Eng.* **2019**, *163*, 114381. https://doi.org/10.1016/j.applthermaleng.2019.114381.
21. Mostafazade Abolmaali, A.; Afshin, H. Development of Nusselt number and friction factor correlations for the shell side of spiral-wound heat exchangers. *Int. J. Therm. Sci.* **2019**, *139*, 105–117. https://doi.org/10.1016/j.ijthermalsci.2019.01.038.
22. Wang, S.; Jian, G.; Xiao, J.; Wen, J.; Zhang, Z. Optimization investigation on configuration parameters of spiral-wound heat exchanger using Genetic Aggregation response surface and Multi-Objective Genetic Algorithm. *Appl. Therm. Eng.* **2017**, *119*, 603–609. https://doi.org/10.1016/j.applthermaleng.2017.03.100.
23. Wang, S.; Jian, G.; Tong, X.; Wen, J.; Tu, J. Effects of spacing bars on the performance of spiral-wound heat exchanger and the fitting of empirical correlations. *Appl. Therm. Eng.* **2018**, *128*, 1351–1358. https://doi.org/10.1016/j.applthermaleng.2017.09.094.
24. Duan, X.; Zhou, A.; Xiao, J.; Wang, S.; Wen, J. Numerical simulation and structure optimization of spiral wound heat exchanger with novel spacing bars. *Can. J. Chem. Eng.* **2024**, *102*, 1341–1352. https://doi.org/10.1002/cjce.25110.
25. Wu, J.; Shao, P.; Yi, J.; Gu, T.; Hou, S.; Gao, C. Numerical study on fluid flow and heat transfer characteristics in spiral wound heat exchanger with helical rods. *Int. Commun. Heat Mass Transf.* **2025**, *167*, 109264. https://doi.org/10.1016/j.icheatmasstransfer.2025.109264.
26. Gu, X.; Jiang, G.; Wo, Y.; Chen, B. Numerical study on heat transfer characteristics of propylene glycol-water mixture in shell side of spiral wound heat exchanger. *Front. Heat Mass Transf.* **2020**, *15*, 1–8. https://doi.org/10.5098/hmt.15.3.
27. Wang, B.; Bi, X.; Sun, N.; Zhang, X.; Wang, T.; Wang, Q. Parametric investigation on shell-side thermohydraulic performance in spiral-wound heat exchangers. *Energy Storage Sav.* **2026**, *5*, 100136. https://doi.org/10.1016/j.enss.2025.12.001.
28. Gao, X.; Zhou, G.; Tu, S. Study on effects of structural parameters on shell-side heat transfer enhancement in spiral wound heat exchangers. *CIESC J.* **2019**, *70*, 2456–2471. (In Chinese) https://doi.org/10.11949/0438-1157.20181534.
29. Wang, Y.; Hou, T.; Cui, C.; Li, Q. Theoretical modeling of process heat transfer mechanism in U-shaped molten salt heat exchanger. *Energy* **2024**, *308*, 132795. https://doi.org/10.1016/j.energy.2024.132795.
30. Bi, X.; Zhang, B.; Guo, Q.; Wang, T.; Guo, W.; Chu, W.; Wang, Q. Thermal performance analysis and parameter optimization of spiral-wound heat exchangers by using local thermal-resistance ratio. *Int. J. Therm. Sci.* **2026**, *229*, 111100. https://doi.org/10.1016/j.ijthermalsci.2026.111100.

31. Fan, J.F.; Ding, W.K.; Zhang, J.F.; He, Y.L.; Tao, W.Q. A performance evaluation plot of enhanced heat transfer techniques oriented for energy-saving. *Int. J. Heat Mass Transf.* **2009**, *52*, 33–44. https://doi.org/10.1016/j.ijheatmasstransfer.2008.07.006.
32. Chen, J.; Huang, T.; Huang, X.; Fang, X.; Ling, Z.; Zhang, Z.; Tang, L. Experimental study and numerical simulation of shell-side heat transfer and flow characteristics of a novel continuous helical baffled heat exchanger without a central tube. *Int. J. Therm. Sci.* **2027**, *232*, 111362. https://doi.org/10.1016/j.ijthermalsci.2026.111362.
33. Zhang, C.; Han, S.; Wu, Y.; Zhang, C.; Guo, H. Investigation on convection heat transfer performance of quaternary mixed molten salt based nanofluids in smooth tube. *Int. J. Therm. Sci.* **2022**, *177*, 107534. https://doi.org/10.1016/j.ijthermalsci.2022.107534.
34. Gnielinski, V. New equations for heat and mass transfer in turbulent pipe and channel flow. *Int. Chem. Eng.* **1976**, *16*, 359–368.
35. Li, J.; Chen, G.; Hu, Y.; Zhang, Z.; Zhao, Z.; Jiang, H.; Li, L. Optimizing turbulent heat transfer modeling of low-Prandtl-number negatively buoyant jets: Data assimilation and solution strategy assessment. *Int. Commun. Heat Mass Transf.* **2026**, *177*, 111522. https://doi.org/10.1016/j.icheatmasstransfer.2026.111522.

Disclaimer/Publisher's Note: The statements, opinions and data contained in all publications are solely those of the individual author(s) and contributor(s) and not of MDPI and/or the editor(s). MDPI and/or the editor(s) disclaim responsibility for any injury to people or property resulting from any ideas, methods, instructions or products referred to in the content.